Monthly Notices
of the
ROYAL ASTRONOMICAL SOCIETY

MNRAS **466,** 4711–4730 (2017)
Advance Access publication 2016 December 24

doi:10.1093/mnras/stw3357

Clouds, Streams and Bridges: redrawing the blueprint of the Magellanic System with *Gaia* DR1

Vasily Belokurov,[1⋆] Denis Erkal,[1⋆] Alis J. Deason,[2] Sergey E. Koposov,[1] Francesca De Angeli,[1] Dafydd Wyn Evans,[1] Filippo Fraternali[3] and Dougal Mackey[4]

[1]*Institute of Astronomy, Madingley Rd, Cambridge CB3 0HA, UK*
[2]*Institute for Computational Cosmology, Department of Physics, University of Durham, South Road, Durham DH1 3LE, UK*
[3]*Department of Physics and Astronomy, University of Bologna, viale Berti Pichat 6/2, I-40127 Bologna, Italy*
[4]*Research School of Astronomy and Astrophysics, Australian National University, Canberra, ACT 2611, Australia*

Accepted 2016 December 20. Received 2016 December 20; in original form 2016 November 15

ABSTRACT

We present the discovery of stellar tidal tails around the Large and the Small Magellanic Clouds (LMC and SMC, respectively) in the *Gaia* DR1 data. In between the Clouds, their tidal arms are stretched towards each other to form an almost continuous stellar bridge. Our analysis relies on the exquisite quality of the *Gaia*'s photometric catalogue to build detailed star-count maps of the Clouds. We demonstrate that the *Gaia* DR1 data can be used to detect variable stars across the whole sky, and, in particular, RR Lyrae stars in and around the LMC and the SMC. Additionally, we use a combination of *Gaia* and *GALEX* to follow the distribution of Young Main Sequence stars in the Magellanic System. Viewed by *Gaia*, the Clouds show unmistakable signs of interaction. Around the LMC, clumps of RR Lyrae are observable as far as $\sim 20^\circ$, in agreement with the most recent map of Mira-like stars reported in Deason et al. The SMC's outer stellar density contours show a characteristic S-shape, symptomatic of the onset of tidal stripping. Beyond several degrees from the centre of the dwarf, the *Gaia* RR Lyrae stars trace the Cloud's trailing arm, extending towards the LMC. This stellar tidal tail mapped with RR Lyrae is not aligned with the gaseous Magellanic Bridge, and is shifted by some $\sim 5^\circ$ from the Young Main Sequence bridge. We use the offset between the bridges to put constraints on the density of the hot gaseous corona of the Milky Way.

Key words: stars: variables: RR Lyrae – galaxies: dwarf – Local Group – Magellanic Clouds – galaxies: structure.

1 INTRODUCTION

'The Magellanic Clouds are a pair of massive dwarf galaxies orbiting the Milky Way'. While seemingly obvious on the surface, the statement above conceals a host of failed observational attempts to verify its parts. Presently, the jury is still debating whether or not the Clouds have been bound to the Galaxy for very long, if at all (Besla et al. 2007; Kallivayalil et al. 2013). The time they have spent as a binary is unknown (see e.g. Besla et al. 2012; Diaz & Bekki 2012), and their masses remain unconstrained, although a coherent picture is starting to emerge in which the Clouds appear much heavier than previously thought (see e.g. van der Marel & Kallivayalil 2014; Peñarrubia et al. 2016). So far, the only fact established with certainty is that the Large and Small Magellanic Cloud (the LMC and the SMC) should not really be here today (Busha et al. 2011; Tollerud et al. 2011). Yet luckier still, the two dwarfs are perfectly positioned for study: close enough so that their individual stars can be resolved and their proper motions measured, but not so close that they cover half of the sky. Having the full view, not just a close-up, is crucial, as the picture of the Magellanic system is complex and filled with scattered intricate details that only make sense in concert. Many of these are in fact signs of the ongoing interaction, both between the Clouds themselves, and of the pair with the Milky Way.

The first observational example of a morphological feature in the SMC most likely caused by its larger neighbour is the eastern stellar 'Wing' discovered by Shapley (1940). The second clue to the Clouds' turbulent relationship is the neutral hydrogen 'bridge' connecting the dwarfs, revealed by the study of Hindman, Kerr & McGee (1963). As Irwin, Kunkel & Demers (1985) showed, this gaseous Magellanic Bridge (MB) is a site of recent star formation, hosting a river of O and B stars, of which the eastern Wing is just the most visible portion. According to the subsequent study of Irwin,

⋆ E-mail: vasily@ast.cam.ac.uk (VB); derkal@ast.cam.ac.uk (DE)

Demers & Kunkel (1990), this river continues the better part of the distance from the Small to the Large Cloud (also see Battinelli & Demers 1992) and possibly even contains a faint 'envelope' of Population II stars. The existence of the young stellar bridge connecting the LMC and the SMC has recently been confirmed by Skowron et al. (2014) using the OGLE's wide and continuous coverage of the area. However, the presence of the recently formed stars in the MB carries little information – besides the important constraint on the time-scale – as to the exact course of the interaction that pulled a great quantity of H I from the SMC to form the bridge itself (for the most recent discussion of the Magellanic gas properties, see the review by D'Onghia & Fox (2016)).

All models agree that the most straightforward way to produce the MB is via tidal stripping of the SMC's gas by the LMC (see e.g. Besla et al. 2012; Diaz & Bekki 2012; Hammer et al. 2015). However, the ferocity of the interaction can be dialled up and down, in accordance with the (poorly known) size and the shape of the SMC's orbit around the LMC. The SMC's orbit is not tightly constrained because the Cloud's relative proper motion has remained uncertain, as have the masses of both dwarfs. Naturally, in the case of a close fly-by, the LMC's tides would also remove some of the SMC's stars. Therefore, the mere existence of the stellar tidal tail corresponding to the gaseous MB may serve as a powerful confirmation of the recent direct interaction. Furthermore, as successfully demonstrated with other Galactic satellites (see e.g. Dehnen et al. 2004; Fellhauer et al. 2007; Gibbons, Belokurov & Evans 2014), tidal streams can also be used to reveal a lot more about the orbital evolution of the Clouds.

The two seminal papers describing the interaction of the Clouds, i.e. Diaz & Bekki (2012) and Besla et al. (2012), both predict stellar tidal tails around the SMC, albeit based on different orbital solutions for the pair. The simulations of Diaz & Bekki (2012) follow a light LMC+SMC pair on multiple passages around the Milky Way. Here, the dwarfs come together as a pair ∼2 Gyr ago and therefore only have enough time for two rendezvous. The most recent encounter between the Clouds, which in this setup happens some 250 Myr ago, creates two prominent – both gaseous and stellar – tidal tails on either side of the SMC. One of these is seen in H I today as the MB and connects the Clouds on the sky and along the line of sight, while the other, dubbed by Diaz & Bekki (2012) the 'counter-bridge', wraps around the SMC and stretches to much larger distance, i.e. ∼90 kpc (see also Muller & Bekki 2007).

Besla et al. (2012) present the results of two Magellanic simulations. In both, the MCs are much heavier compared to the model of Diaz & Bekki (2012) and have just passed their first pericentre around the Galaxy. However, contrary to the model of Diaz & Bekki (2012), the Clouds are allowed to interact with each other for a much longer period. The intensity of this interaction is different for the two models of Besla et al. (2012): Model 1 has a large pericentric distance of the SMC around the LMC, of the order of ∼30 kpc, while in Model 2, there is a direct collision between the dwarfs. Accordingly, the gaseous MB appears rather weak in Model 1 and very dramatic in Model 2. The difference in the MB gas contents in the two models is also reflected in the distinct star-forming properties of the Bridge: in Model 1 the density of neutral hydrogen is too low to kick-start star production, while in Model 2, there is copious *in situ* MB star formation. Note, however, that the amount of the stripped MB stellar debris in Model 2 does not necessarily match the high gas density. This is because, during the collision, the SMC's gas is stripped not only by the LMC's tidal force but also by the ram pressure of its gaseous disc. Nevertheless, as the follow-up treatise by Besla, Hernquist & Loeb (2013) demonstrates, Model 2 predicts a factor of ∼5 more old stellar (e.g. RR Lyrae stars) tidal debris in the MB compared to Model 1 (see their table 5).

As both Diaz & Bekki (2012) and Besla et al. (2012), as well as a string of authors before them, predict a stellar counter-part to the gaseous MB, the region between the Clouds corresponding to the highest H I column density has been trawled thoroughly for the tidally stripped SMC stars. The results of the search are somewhat inconclusive. For example, Demers & Battinelli (1998) and Harris (2007) conclude that the stellar population of the MB is predominantly young and very little, if any, stellar material has been stripped from the SMC. On the other hand, Kunkel, Demers & Irwin (2000), Nidever et al. (2013), Bagheri, Cioni & Napiwotzki (2013), Skowron et al. (2014) and Noël et al. (2015) all find evidence of an intermediate-age stellar population in the MB area.

In this paper, we take advantage of the unique photometric data set, provided as part of the *Gaia* Data Release 1 (GDR1), to study the low-surface-brightness stellar density field around the Magellanic Clouds. *Gaia* is the European Space Agency's project to create a detailed map of the Galactic stellar distribution. *Gaia* scans the entire sky constantly, thus providing a record of stellar positions and fluxes, as well as tangential motions and flux variations over a period of 5 years with a typical temporal sampling window of ∼1 month. *Gaia*'s limiting magnitude in a very wide optical G band is ∼20.5 which is similar to the limiting magnitude ($I \sim 21$) of the OGLE IV survey,[1] which before 2016 Sept 14 provided the widest coverage of the Magellanic system at this depth.

This paper is organized as follows. Section 2 describes the behaviour of the Galactic dust reddening in the *Gaia* G band around the Magellanic Clouds and presents the star-count maps of both dwarfs. Section 3 introduces the *Gaia* variability statistics and discusses how genuine variable stars can be distinguished from artefacts. We kindly warn the reader that parts of this section are rather technical, and those mostly interested in the properties of the Magellanic Clouds rather than the particularities of the *Gaia*'s photometry might like to skip straight to the next section. Section 4 presents the discovery of the trailing tidal tail of the SMC and a new map of the Young stellar bridge traced with a combination of *Gaia* and *GALEX*. Finally, Section 5 puts the discovery into context.

2 MAGELLANIC CLOUDS IN *GAIA* DR1

The analysis reported below relies on the all-sky source table GaiaSource released as part of the *Gaia* DR1 (see Brown et al. 2016; van Leeuwen et al. 2016, for details).

2.1 Extinction

Before any examination of the *Gaia* photometry can be carried out, the apparent magnitudes must be corrected for the effects of Galactic dust extinction. The LMC's Galactic latitude is only $b \sim -30^\circ$ and there are plenty of filamentary dust patches with high reddening levels in its vicinity. *Gaia*'s G band is very wide and therefore the conversion from $E(B-V)$ to extinction A_G is a complex function of the source's spectral energy distribution. For the analysis presented here, this prescription can be simplified as we are concerned with stars in a narrow range of colour, i.e. $0.2 < B - V < 0.4$ (see e.g. Catelan 2009, for details). Based on the pre-flight simulations, Jordi et al. (2010) recommend $A_G/E(B-V) \sim 3$ for stars with

[1] http://ogle.astrouw.edu.pl/.

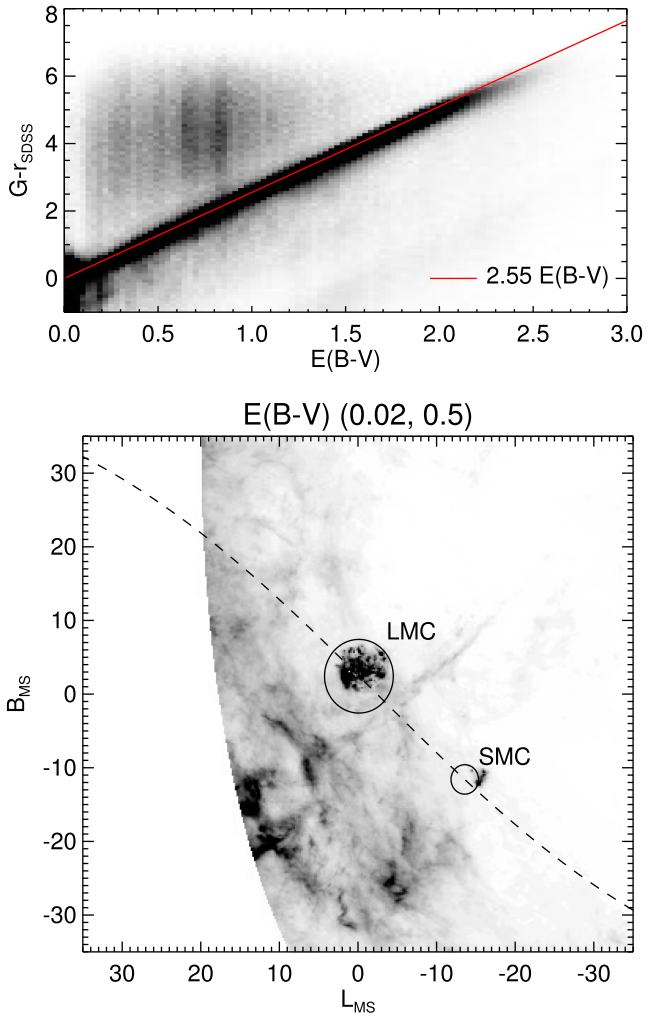

Figure 1. Top: density of stars with both SDSS and *Gaia* measurements and $(g - r)_{\rm SDSS} < 0.3$, in the plane of $G - r_{\rm SDSS}$ and $E(B - V)$. G is not corrected for dust reddening, but $r_{\rm SDSS}$ is. The solid red line shows that $A_G = 2.55E(B - V)$ provides a reasonable fit to the bulk of the data. The obvious outliers from this relationship are the small number of blended stars (as seen by the SDSS). Bottom: the distribution of the dust extinction from Schlegel et al. (1998) in the MS coordinates for locations with Galactic $b < -15°$. The black dashed line is the equator of the MB coordinate system. The black circle with a radius of 5° (2°) marks the location of the LMC (SMC).

colours consistent with those of RR Lyrae (see top left panel of their fig. 17).

With the GDR1 in hand, it is now possible to estimate the extinction coefficient, A_G, directly from the data. Here, we do it by simply comparing the uncorrected G magnitude to de-reddened Sloan Digital Sky Survey (SDSS) r-band magnitude for all stars measured by both *Gaia* and SDSS as a function of $E(B - V)$. Here, we use the SDSS r band as it is closely related to the *Gaia* G band. The result of this comparison is shown in Fig. 1, where the following relationship appears to hold true:

$$A_G = 2.55E(B - V). \quad (1)$$

Reassuringly, this is not too far from the value suggested by Jordi et al. (2010) based on the theoretical calculations. In the analysis that follows, the G-band magnitudes are de-reddened using the conversion above. We have also checked the behaviour of A_G for stars in other colour regimes, and equation (1) appears to work well, albeit with increased scatter.

2.2 Magellanic stream and MB coordinate systems

The bottom panel of Fig. 1 displays the Galactic dust map as calculated by Schlegel, Finkbeiner & Davis (1998) in the Magellanic Stream (MS) coordinates. This coordinate system is suggested by Nidever, Majewski & Burton (2008) and is approximately aligned with the extended trailing tail of neutral hydrogen emanating from the Clouds. The Galactic coordinates can be converted into the MS longitude $L_{\rm MS}$ and latitude $B_{\rm MS}$ by aligning with a great circle with a pole at $(l, b) = (188.^\circ5, -7.^\circ5)$. Note that in the MS system, the LMC lies slightly off-centre and has coordinates $(L_{\rm MS}, B_{\rm MS}) = (-0.^\circ14, 2.^\circ43)$, while the SMC is positioned at $(L_{\rm MS}, B_{\rm MS}) = (-15.^\circ53, -11.^\circ58)$.

The dashed line in the bottom panel of Fig. 1 indicates the equator of a different coordinate system in which both the LMC and the SMC have zero latitude. We call this system the MB coordinates as its equator aligns well the H I bridge (see Section 4.3). The equatorial coordinates can be converted into the MB longitude $X_{\rm MB}$ and latitude $Y_{\rm MB}$ by aligning with a great circle with a pole at $(\alpha, \delta) = (39.^\circ5, 15.^\circ475)$. In this new MB coordinate system, the LMC is at $(X_{\rm MB}, Y_{\rm MB}) = (0°, 0°)$ and the SMC is at $(X_{\rm MB}, Y_{\rm MB}) = (-20.^\circ75, 0°)$.

2.3 Star-count maps

Fig. 2 gives the density distribution of all stars in the GDR1's GaiaSource table with $11 < G < 19.5$ in the MB coordinate system. From top to bottom, the density distribution remains the same, but the dynamic range of the grey-scale image is varied. The top panel highlights the high-density regions, while the second from bottom panel emphasizes the low-surface-brightness environs of the Clouds. Finally, the bottom panel attempts to summarize the behaviour of the stellar density across all surface-brightness levels. Note that a simple model of the Galactic foreground/background has been subtracted from these stellar density maps. Namely, the number counts in the range $-13° < X_{\rm MB} < 35°$, but excluding $-8° < X_{\rm MB} < 8°$, were modelled as a quadratic polynomial of $Y_{\rm MB}$. The parameters of the model were constrained independently for each pixel column.

As illustrated in the figure, the LMC star-count distribution harbours a dense central core with a number of clumpy (presumably star-forming) regions, surrounded by an irregularly shaped spiral or ring-like pattern. The shape and the position angle of the LMC's iso-density contours evolve from the centre outwards. In this map, the LMC can be seen as far as $X_{\rm MB} \sim 9°$ in the East and $X_{\rm MB} = -8°$ in the West. Overall, this view of the LMC appears remarkably similar to that published recently by Besla et al. (2016). The first two panels show several small-scale features in the SMC: most notably, the 47 Tuc globular cluster in the West and the Wing in the East. The pointy tip of the Wing at $(X_{\rm MB}, Y_{\rm MB}) = (-15°, 0°)$ remains a dramatic feature in all panels of the figure.

A substantial twist in the SMC's iso-density contours can be seen in the third (or second from bottom) panel. Here, the outer stellar density distribution appears to have the characteristic S-shape, typical of the tidal tails around disrupting satellites (see e.g. Odenkirchen et al. 2001). In this picture, the SMC tails appear rather stubby and drop out of sight around ∼6° away from the satellite. The orientation of the two tails seem to be well-aligned with the SMC's relative (to the LMC) proper motion vector, shown as

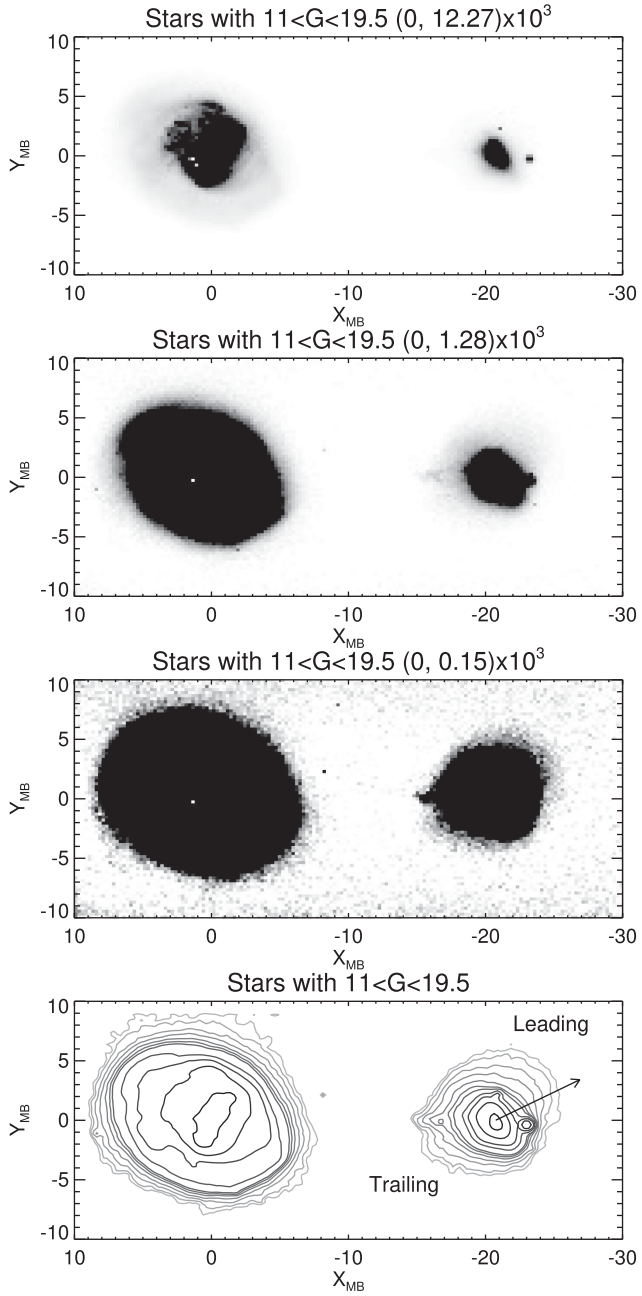

Figure 2. Density of stars with $11 < G < 19.5$ in the MB coordinate system. The pixels are $0.^{\circ}25 \times 0.^{\circ}25$. A background model comprising a quadratic polynomial for each column (constrained over the range of $-13^{\circ} < X_{\rm MB} < 35^{\circ}$, but excluding $-8^{\circ} < X_{\rm MB} < 8^{\circ}$) is subtracted. Across all panels, the density distribution is the same, only the dynamic range of the pixel values changes. The number of stars corresponding to white (low counts) and black (high counts) levels is shown in brackets in the title of each panel. First (top) panel: note the perturbed disc of the LMC. Second panel: note the low surface-brightness extension of the SMC, the 47 Tuc cluster in the western part of the dwarf and the Wing in the eastern side, facing the LMC. Third panel: note the characteristic S-shape of the outer envelope of the density distribution of the SMC. Fourth (bottom) panel: note the twist of the iso-density contours from the centre outwards. The two protruding ends of the S-shape are the origins of the SMC tidal tails. The arrow shows the Cloud's proper motion relative to the LMC as computed using the values from Kallivayalil et al. (2013). The solar reflex motion is subtracted. The leading and trailing tails are marked taking into account the direction of the SMC's motion around the LMC.

an arrow in the bottom panel of the figure. Given the direction of the Cloud's motion, we designate the tail stretching towards the top right or $(X_{\rm MB}, Y_{\rm MB}) = (-24^{\circ}, 5^{\circ})$ as leading, and the tail pointing towards the LMC, more precisely towards $(X_{\rm MB}, Y_{\rm MB}) = (-16^{\circ}, -3^{\circ})$, as trailing. Note that the twisting/elongation of the SMC density contours is in broad agreement with the earlier studies of the dwarf using tracers like Cepheids, Red Clump stars and RR Lyrae and is intimately linked to its changing extent along the line of sight (see e.g. Nidever et al. 2013; Jacyszyn-Dobrzeniecka et al. 2016; Scowcroft et al. 2016).

3 MAGELLANIC RR LYRAE IN *GAIA* DR1

3.1 Variable stars in *Gaia* DR1

Gaia is a variable star machine. By scanning the entire sky multiple times over a baseline of many years, it reveals objects that change brightness across a wide range of time-scales and amplitudes. As displayed by the sample of the LMC RR Lyrae and Cepheids published as part of GDR1, the quality of the *Gaia* light curves is exquisite and is bested only by *Kepler*. While the deluge of the all-sky variability data is expected to be unleashed in the coming data releases, the GDR1's GaiaSource (GSDR1) table contains enough information to identify objects whose flux changes with time and even group them broadly into classes.

Fig. 3 shows the distribution of previously identified variables sorted according to their type in the plane of the variability amplitude statistic Amp (see below) as a function of the *Gaia* G magnitude. This variability amplitude estimate relies on the fact that GSDR1 reports the mean flux as well as the error of the mean flux estimate. The flux error is defined as the error on the weighted mean flux computed using all available epoch data for a given source (see Carrasco et al. 2016). For variable sources, the mean flux error gauges the range of oscillation in the object's flux. Therefore, for each source in GSDR1, we can define Amp as follows:

$$\mathrm{Amp} = \log_{10}\left(\sqrt{N_{\rm obs}}\frac{\sigma_{\overline{I_G}}}{\overline{I_G}}\right). \quad (2)$$

Here, $N_{\rm obs}$ is the number of CCD crossings, $\sigma_{\overline{I_G}}$ is the mean G flux error and $\overline{I_G}$ is the mean G-band flux. Fig. 3 presents the GSDR1 view of several of the familiar classes of variable stars residing in the Magellanic Clouds, such as the LMC Cepheids (yellow, top left) from Soszynski et al. (2008), long-period semi-regular variables (SRVs; orange, top centre) and Mira stars in the LMC (red, top right) from Soszyński et al. (2009), LMC eclipsing binaries (green, middle left) from Graczyk et al. (2011), the SMC eclipsing binaries (green, middle centre) from Pawlak et al. (2013), LMC RR Lyrae (blue, bottom left) and SMC RR Lyrae (purple, bottom centre) from Soszyński et al. (2010). Also shown are the QSO and AGN (black, middle right) from Véron-Cetty & Véron (2010). It helps enormously that all of the stellar variables above are located at approximately the same heliocentric distance. Therefore, for many of these, the G magnitude distribution is simplified, as illustrated by the clustering of the LMC Cepheids and LPVs. The clustering is most pronounced for the RR Lyrae: for these pulsators, the amplitude–luminosity relation induces only a modest change in the apparent magnitude.

Motivated by the tight bunching of the previously identified Magellanic RR Lyrae in the (G, Amp) space, we propose a simple selection box shown in the right panel of the bottom row of Fig. 3. Sources above the diagonal line are predicted to exhibit variability larger than expected for a constant star at the given G magnitude.

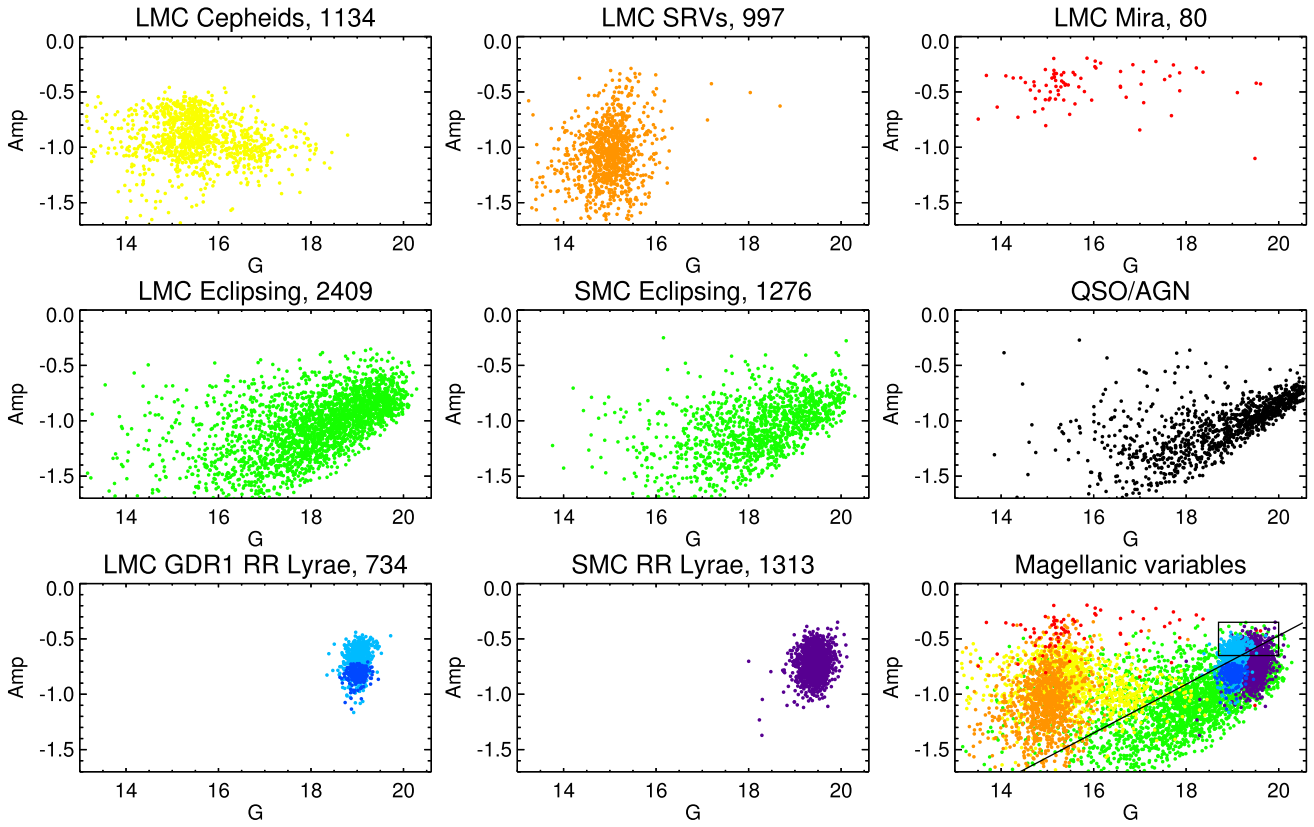

Figure 3. Variable sources in *Gaia* DR1. Previously identified objects with secure classification are shown in the plane spanned by the variability amplitude Amp and the *Gaia* magnitude G. The title also reports the number of variables shown. Top left: LMC Cepheids with $3^\circ < D_{\rm LMC} < 10^\circ$ from Soszynski et al. (2008). Top centre and right: long-period SRVs and Mira stars in the LMC from Soszyński et al. (2009) with $3^\circ < D_{\rm LMC} < 10^\circ$. Middle left: LMC eclipsing binaries with $3^\circ < D_{\rm LMC} < 10^\circ$ from Graczyk et al. (2011). Middle centre: SMC eclipsing binaries with $D_{\rm SMC} > 1^\circ$ from Pawlak et al. (2013). Middle right: QSO and AGN from Véron-Cetty & Véron (2010). Bottom left: *Gaia* DR1 RR Lyrae with $5^\circ < D_{\rm LMC} < 10^\circ$ (see Clementini et al. 2016, for details). RRab (RRc) stars are shown in light (dark) blue. Bottom centre: RR Lyrae in the SMC with $D_{\rm SMC} > 1^\circ$ from Soszyński et al. (2010). Bottom right: all Magellanic variables from other panels. Black lines show the RR Lyrae selection boundaries used in the analysis. This selection yields 38 per cent completeness for the LMC RR Lyrae and 13 per cent completeness for the SMC RR Lyrae. Note that the variables shown in this figure also had to pass the additional cuts detailed in Section 3.3.

Note that this is a conservative variability threshold and most non-variable sources have much lower Amp values (at given magnitude). However, we believe this choice is warranted given the GSDR1 teething problems with the source cross-match (see Section 3.2 for details). The diagonal line slices through the cloud of RR Lyrae approximately where the RRab and the RRc pulsators separate (for the LMC, these are indicated with different shades of blue). Therefore, our RR Lyrae sample consists almost entirely of the RR Lyrae of the ab type. The vertical boundaries are chosen to include both the LMC and the SMC RR Lyrae. Note that the apparent magnitude of the RR Lyrae in the LMC is offset ∼0.5 mag brighter compared to that of the SMC. This reflects the difference in the line-of-sight distance to the Clouds: the LMC is at 49.97 kpc (see Pietrzyński et al. 2013) and the SMC is at 62.1 kpc (see Graczyk et al. 2014). Converted into distance moduli, these correspond to 18.509 and 18.965 for the LMC and the SMC, respectively. It is clear from the figure that the selection proposed is neither complete nor pure. The objects chosen using this simple boundary will not be limited to the Magellanic RR Lyrae exclusively: some of the Magellanic eclipsing binaries will also be included. Additionally, a small number of variable QSO and AGN can pass these variability cuts too. We discuss the sample's completeness and purity in Section 3.3.

3.2 Selection biases, galaxies and artefacts

Having glanced at the distribution of genuine variable stars in the plane of (G, Amp), let us inspect the behaviour of the bulk of the *Gaia* sources in and around the Clouds. Fig. 4 presents (the logarithm of) the density of sources in the (G, Amp) space for a $70^\circ \times 70^\circ$ region centred on $(L_{\rm MS}, B_{\rm MS}) = (0^\circ, 0^\circ)$. More precisely, the first panel gives the view of the foreground/background as the Clouds themselves are excised from this picture, while the second and the third panels display stars in the LMC and the SMC, respectively. As predicted above, most stars lie well below the diagonal line segregating variable and non-variable objects. Additionally, in the leftmost panel, very few stars enter the Magellanic RR Lyrae box in the top right corner of the plot. The second and third panels confirm that this box is populated with RR Lyrae stars, whose magnitude distributions are offset with respect to each other due to the difference in the heliocentric distances of the Clouds as discussed in Section 3.1.

Apart from the many expected features, the distributions shown in the first three panels of Fig. 4 also reveal several odd-looking sub-structures, many of which run diagonally across the (G, Amp) plane over a wide range of magnitudes. We believe that most of these sharp over-densities in the variability–magnitude space are

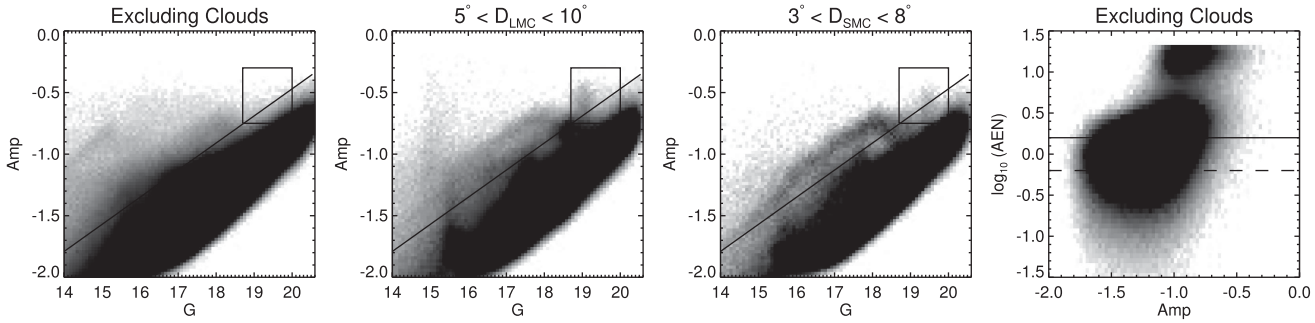

Figure 4. True and spurious variable objects in *Gaia* DR1. The first three panels show the logarithm of density of objects in (Amp, G) space. The first panel shows stars in a $80^\circ \times 80^\circ$ region centred on the LMC, but with the area around the LMC and the SMC and below Galactic $b = 20^\circ$ excluded. The second (third) panel presents the stars around the LMC (SMC). Stars below the black diagonal line are mostly constant, while those above it appear variable (approximately 3.9 million in this area) in *Gaia* DR1. While some of the genuine variable stars do cluster in this space, e.g. RR Lyrae (see Fig. 3), mostly, these do not produce well-defined sequences spanning large ranges of magnitude. Much of the clustering visible in these panels is due to spurious 'variables' likely caused by cross-match failures. Note that our final RR Lyrae selection box avoids the vast majority of the prominent artefacts visible in the first three panels. The fourth panel gives the logarithm of density of stars in the space of (the logarithm of) excess astrometric noise, AEN, and variability amplitude, Amp, for objects with $18.7 < G < 20$, i.e. those in the RR Lyrae selection range. The stand-alone cloud with large $\log_{10}$(AEN) is mostly galaxies. Our working hypothesis is that the objects with cross-match problems appear as spurious photometric variables with large AEN. Therefore, we exclude a chunk of (AEN, Amp) space in which the two correlate. Using a conservative cut of $\log_{10}(\mathrm{AEN}) < 0.25$ (black horizontal line) leaves 2.9 million variable objects, while a strict cut of $\log_{10}(\mathrm{AEN}) < -0.2$ leaves 1.6 million variable stars.

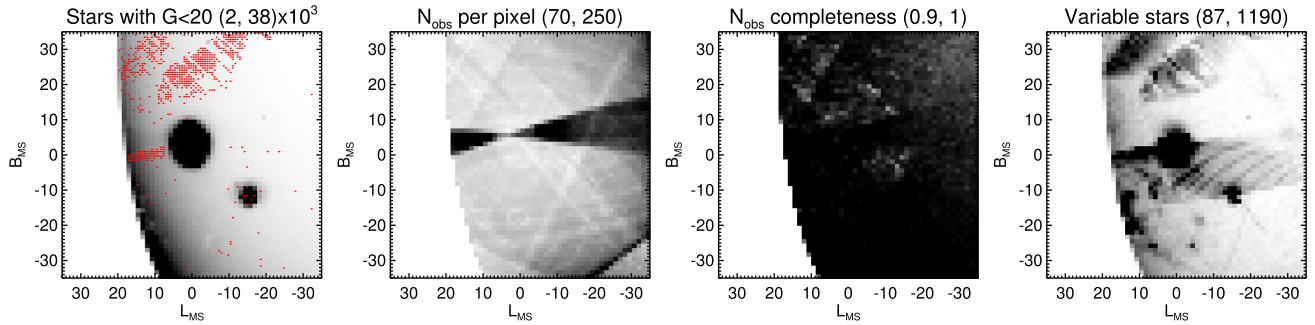

Figure 5. Statistics of the *Gaia* DR1 observations of the Magellanic system. This shows the $70^\circ \times 70^\circ$ area centred on the LMC in the MS coordinate system. Density maps have pixels with $1^\circ\!.25$ on a side. The pixel values corresponding to black and white are given in brackets in the title of each panel. First panel: number density of stars with $G < 20$. Small red dots mark the pixels identified as strongly affected by the cross-match failures and excluded from the subsequent analysis. Second panel: mean number of CCD transits per pixel on the sky. Note the dark region corresponding to the Ecliptic Pole scanning. Third panel: completeness due to $N_{\rm obs} > 70$ cut. Fourth panel: density of 'variable' sources using the cut shown in Fig. 4. Note that apart from the LMC and the SMC, a number of over-dense regions appear. These are the portions of the *Gaia* DR1 sky most affected by cross-match failures.

spurious, and are caused by cross-match failures in the GSDR1. This is confirmed in the rightmost panel of Fig. 5 where the on-sky density distribution of all nominally variable objects (i.e. stars above the black diagonal line) is displayed. Apart from the obvious over-densities clearly associated with the LMC and the SMC, there are many regions with sharply defined boundaries with a strong excess of 'variable' objects. Fig. 6 provides further insight into the nature of these artefacts. The figure zooms in on to several over-dense regions visible in the right panel of Fig. 5 and shows that these over-densities resolve into thin, mostly well-aligned strips. For the $10^\circ \times 10^\circ$ region centred on $(L_{\rm MS}, B_{\rm MS}) = (-25^\circ, -5^\circ)$ (shown in the first and second panels of Fig. 6), the strips are less than a degree wide [in fact, their cross-section approximately matches the *Gaia*'s field of view (FoV) size of $0^\circ\!.65$] and the separation between the strips appears constant and equal to $\sim 5^\circ$. Given the tight alignment between the strips, it seems likely that the problem occurred over a small range of epochs. Given the sharp diagonal sequence sitting above the variable selection line and turning over at $G \sim 18$ (see left panel of the figure), it appears that stars over a wide range of magnitudes were affected. Based on the diagnostics presented in Figs 5 and 6, we conjecture that a fault in the object cross-match procedure is the cause of these spurious features. At a small number of epochs (as indicated by the sparseness of the strips), stars were assigned flux from unrelated objects, thus making the otherwise non-variable sources appear 'variable'.

In the presence of these striking artefacts, it is comforting to see that very few spurious objects seem to have entered the designated RR Lyrae box. Bear in mind, however, that the exact pattern of spurious features changes from location to location as displayed in the third and fourth panels of Fig. 6 where stars from the region centred on $(L_{\rm MS}, B_{\rm MS}) = (0^\circ, 25^\circ)$ are shown. Here, the width and the distance between the strips seem to be variable, indicating that the cross-match has likely faltered for objects observed at several epochs (or ranges of epochs). In the amplitude–magnitude space, the familiar diagonal feature is visible, although it seems to be less pronounced at $G > 18$. Nonetheless, the RR Lyrae box appears to be slightly more contaminated compared to the levels seen for the stars in the $(L_{\rm MS}, B_{\rm MS}) = (-25^\circ, -5^\circ)$ region.

If the problems with the GSDR1 source cross-match are the cause of the spurious variability discussed above, then the objects affected

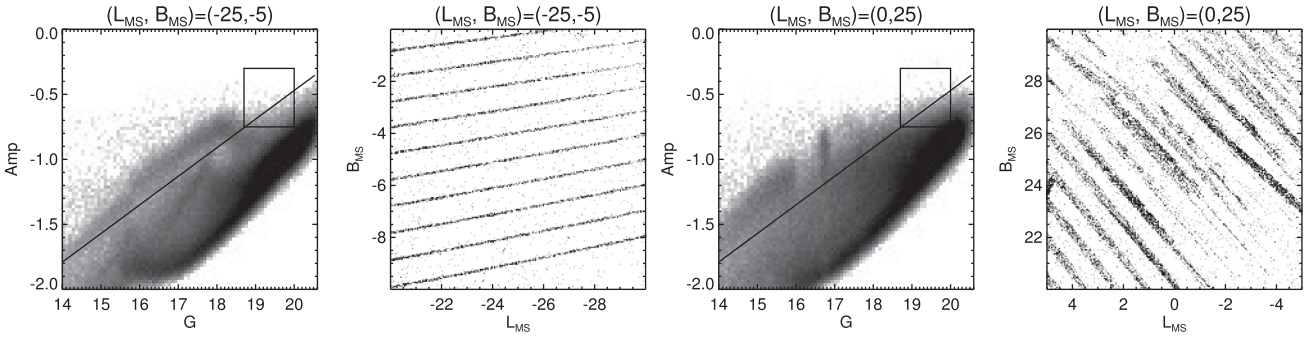

Figure 6. Examples of the *Gaia* cross-match failures in selected $10^\circ \times 10^\circ$ areas around the Magellanic Clouds. First and third panels: density of stars in the plane of Amp and G magnitude for the location with coordinates given in the title of the panel. Note the sharp diagonal features symptomatic of flux mis-allocation. Variable stars are required to lie above the black diagonal line, while the Magellanic RR Lyrae must also be within the black box shown in top right corner. Second and fourth panels: on-sky density distribution of 'variable' stars in the area centred in the location given in the title of the panel. The *Gaia* scanning pattern is clearly visible, thus emphasizing the spurious nature of many of the stars identified as 'variable' in these regions.

ought to exhibit abnormal astrometric behaviour as well. This seems indeed to be the case as illustrated in the rightmost panel of Fig. 4. Here (the logarithm of) the astrometric excess noise is shown as a function of the variability amplitude Amp for stars with magnitudes consistent with the Magellanic RR Lyrae. The objects appear to sit in two separate clusters in this 2D plane: the one that stretches upward from low to high AEN values, and the one which seems to be composed only of objects with high AEN. By examining the catalogues of the *Gaia* sources observed by the SDSS, it has become clear that the latter (the isolated cloud of high AEN objects) mostly consists of galaxies (or, perhaps, their central compact and high surface-brightness parts). Note that the larger sequence, sitting below the galaxy cloud, appears to change its shape as a function of Amp: in other words, there is a noticeable correlation between the photometric variability and poor astrometric fit, especially for objects with $\log_{10}(\mathrm{AEN}) > 0.2$. Therefore, we choose to cull the contaminating galaxies as well as the objects most affected by cross-match failures by requiring $\log_{10}(\mathrm{AEN})$ to be lower than a certain threshold value, the choice for which is discussed below.

A distinctive feature of the *Gaia* mission is the non-uniformity of the sky coverage. The *Gaia*'s scanning law produces strong patterns on the celestial sphere in terms of the numbers of visits per location. At the time of the GSDR1 release, some corners of the Galaxy barely had 10 *Gaia* observations. The number of visits not only determines the overall depth of the G-band photometry, but also controls the significance of the source's variability. Moreover, the variability statistic Amp will evolve as the number of observations grows, depending on the shape of the light curve and the period of the star. The second panel of Fig. 5 shows the average number of CCD observations per pixel on the sky. The strongest feature is the ecliptic scan region which was repeatedly imaged by *Gaia* at the beginning of the mission. The map shows changes in N_{obs} per source across the sky, i.e. the number of individual CCD transits. Given that the *Gaia*'s focal plane contains an array of nine CCDs, this number must be divided by nine to get an approximate number of visits of the given object. The number of visits is likely lower for fainter stars as they may not be detected in every FoV transit and it is more likely that, due to the priority given to brighter objects, they may not be allocated a window. As the figure demonstrates, while the variation in the number of observations is markedly apparent, most stars around the Magellanic Clouds have traversed the *Gaia*'s focal plane at least eight times ($N_{\mathrm{obs}} > 70$). Indeed, as the third panel demonstrates, requesting the minimal of $N_{\mathrm{obs}} = 70$ induces only minor incompleteness, which can easily be corrected for.

3.3 Magellanic RR Lyrae sample

Guided by the GSDR1 properties of known variable stars as well as the behaviour of the data as a function of the number of observations and the resilience of the variability statistic against the artefacts induced by the failures of the cross-match procedure, we put forward the following selection cuts aimed to produce a sample of RR Lyrae candidates around the LMC and the SMC.

$$\begin{aligned}
&\mathrm{Amp} > 0.22G - 4.87 && i\\
&\left.\begin{array}{rl}\log_{10}(\mathrm{AEN}) < 0.2, & \text{weak}\\ \log_{10}(\mathrm{AEN}) < -0.2, & \text{strict}\end{array}\right\} && ii\\
&18.7 < G < 20.0 && iii\\
&N_{\mathrm{obs}} > 70 && iv\\
&E(B-V) < 0.25 && v\\
&\left.\begin{array}{rl}-0.75 < \mathrm{Amp} < -0.3, & \text{weak}\\ -0.65 < \mathrm{Amp} < -0.3, & \text{strict}\end{array}\right\} && vi\\
&b < -15^\circ && vii.
\end{aligned} \tag{3}$$

The first cut selects the likely variable objects; the second one gets rid of galaxies and the objects most affected by cross-match failures – this cut be made stronger if a cleaner sample of RR Lyrae is required; the third one limits the magnitude range to that populated by the LMC and the SMC RR Lyrae; the fourth requires at least eight visits to the given location; the fifth eliminates the areas most affected by the Galactic dust (note that this cut is only applied outside of a 4° radius from the LMC's centre); the sixth cut limits the overall variability amplitude; finally, the seventh cut gets rid of the fields too close to the Galaxy's disc. Additionally, there are two areas in the vicinity of the LMC that are affected by the presence of spurious variables more than others. This is (i) an area with $15^\circ < L_{\mathrm{MS}} < 5^\circ$ visible as a dark thin bar to the left of the LMC in the rightmost panel of Fig. 5 and (ii) the area around $(L_{\mathrm{MS}}, B_{\mathrm{MS}}) \sim (-5^\circ, 25^\circ)$ with a pattern of artefacts displayed in the third and fourth panels of Fig. 6.[2] We eliminate a small number of the most affected pixels in these two areas as follows. Given that very few genuine variable stars exhibit variability levels higher than

[2] This area is only few degrees away from the second brightest star on the sky, Canopus, and therefore may have been affected by the star's ghost images.

Amp $= -0.4$ at $G > 19$, we create a map of number counts of stars with $-0.37 <$ Amp < 0.5 and $19 < G < 20.5$ and cull all pixels with values above the 95th percentile. As shown in the third panel of Fig. 6, the second most affected area has a sharp feature in the (G, Amp) space at $G \sim 17$. Therefore, we build a map of number counts of stars with $-1 <$ Amp < -0.8 and $16.7 < G < 16.9$ and get rid of pixels with values above the 95th percentile. All of the affected pixels are marked with red dots in the left panel of Fig. 5.

The combination of the first and the last cut in equation (3) yields $\sim 3.9 \times 10^6$ objects in the $80^\circ \times 80^\circ$ area around the LMC. If in addition a weak (strict) cut on AEN is imposed, the number of variable objects shrinks to $\sim 2.8 \times 10^6$ ($\sim 1.6 \times 10^6$) sources. The sample shrinks drastically if these two criteria are applied in combination with the magnitude cut, leaving a total of 67 000 likely variable objects with magnitudes consistent with Magellanic RR Lyrae. The application of all cuts in equation (3) as well as the masking of bad pixels described above produces the final sample of ∼21 500 RR Lyrae candidates. These numbers are consistent with the expectation for the total number of RR Lyrae around the Clouds. For example, Soszyński et al. (2016) report some 45 000 RR Lyrae found as part of the OGLE-IV Magellanic campaign. Our sample is smaller even though the area covered is significantly larger. This is because the completeness of our selection is far from 100 per cent as indicated by the diagonal line slicing right through the clusters of RR Lyrae in Fig. 3. Additionally, given that this line passes through the SMC RR Lyrae at higher values of Amp, the completeness of the SMC RR Lyrae sample is expected to be lower than that of the LMC. We estimate the completeness of our selection by counting the number of the previously identified RR Lyrae stars recovered around the LMC and the SMC. Namely, we detect ∼38 per cent of the LMC RR Lyrae reported as part of the GDR1 (see Clementini et al. 2016, for details) and ∼12 per cent of the SMC RR Lyrae discovered by Soszyński et al. (2010). The above numbers are for the 'weak' $\log_{10}$(AEN) < 0.2 cut. If a 'strict' $\log_{10}$(AEN) < -0.2 cut is applied, the completeness drops to ∼13 per cent and ∼8 per cent, respectively. As shown below, an alternative RR Lyrae selection can be used, where the amplitude cut is tightened to Amp > -0.65 while keeping the weak cut on astrometric excess noise ($\log_{10}$(AEN) < 0.3): the completeness of this selection is ∼30 per cent and ∼11 per cent for the LMC and the SMC RR Lyrae correspondingly. Finally, if strict cuts are used for both variability and amplitude, the completeness is minimal at the level of <10 per cent for both the LMC and the SMC RR Lyrae.

The contamination of the GSDR1 RR Lyrae sample can be gauged by counting the number of stars classified as RR Lyrae candidates using GSDR1 information only, but not by other variability surveys. This procedure can only be implemented in the vicinity of the LMC and the SMC where published RR Lyrae data sets exist. Using the samples presented by Clementini et al. (2016) and Soszyński et al. (2010), the contamination of the RR Lyrae sample analysed here is between 30 and 40 per cent. This is much worse than is typically achieved by targeted RR Lyrae searches (see e.g. Drake et al. 2013; Torrealba et al. 2015; Hernitschek et al. 2016). Nonetheless, the purity of our RR Lyrae selection is higher than that of samples of distant Blue Horizontal Branch (BHB) stars assembled using deep broad-band photometry with surveys such as SDSS and DES (see e.g. Deason et al. 2012, 2014; Belokurov et al. 2014; Belokurov & Koposov 2016).

The GSDR1 RR Lyrae sample purity as estimated above does not vary dramatically as the Amp and AEN cuts are changed from weaker to stronger. However, the excess of spurious variable stars in areas affected by cross-match failures can be reduced significantly

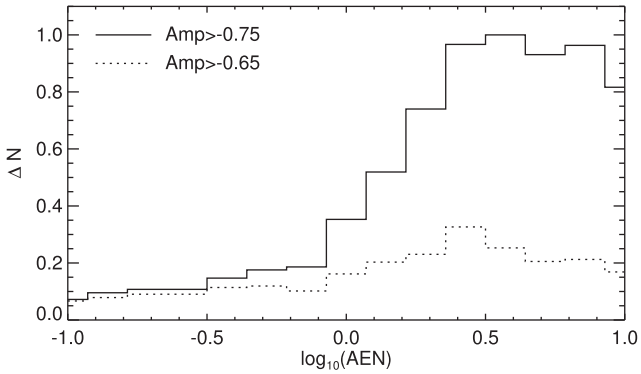

Figure 7. Excess of spurious variable stars as a function of the $\log_{10}$(AEN) threshold for two different variability amplitude cuts. This shows the difference in the number of stars in an area around ($L_{\rm MS}$, $B_{\rm MS}$) = (25°, −5°) (see Fig. 6) compared to an area largely unaffected by cross-match breakdown, namely ($L_{\rm MS}$, $B_{\rm MS}$) = (−25°, −25°). If Amp > -0.75 cut is imposed, then a cut of $\log_{10}$(AEN) < 0.2 gets rid of ∼50 per cent of the spurious variables, while $\log_{10}$(AEN) < -0.2 only leaves ∼15 per cent artefact contamination. Note that a similar level of ∼15 per cent can be achieved with Amp > -0.65 and $\log_{10}$(AEN) < 0.3 cuts.

by dialling the variability amplitude and the astrometric excess noise thresholds. This is illustrated in Fig. 7. Here, the excess of RR Lyrae candidate stars in the problematic area centred on ($L_{\rm MS}$, $B_{\rm MS}$) = (−25°, −5°) with respect to the count in a relatively unaffected area around ($L_{\rm MS}$, $B_{\rm MS}$) = (−25°, −25°) is shown as a function of the AEN cut for two different Amp choices. As shown in the figure, with Amp > -0.75, the weak cut $\log_{10}$(AEN) < -0.2 gets rid of ∼50 per cent of the spurious excess (black solid line). Making the AEN criterion stricter, i.e. $\log_{10}$(AEN) < -0.2 leaves only <20 per cent contamination. On the other hand, similar purity in this area can be achieved if the variability amplitude threshold is higher at Amp > -0.65 and $\log_{10}$(AEN) < 0.3. The two choices for the combination of the Amp and the $\log_{10}$(AEN) cuts deliver similar levels of purity in the cross-match affected areas, albeit the latter yields a higher completeness (as described above). In what follows, we use different combinations of Amp and the $\log_{10}$(AEN) thresholds and explore how the properties of the outer environs of the LMC and the SMC change as the completeness and the purity of GSDR1 sample of RR Lyrae evolve.

4 THE MAGELLANIC BRIDGES

4.1 The RR Lyrae bridge

Fig. 8 shows the density of the GSDR1 RR Lyrae candidate stars in the MS coordinate system. These are selected using the criteria presented in equation (3), in particular by applying the weak cut on variability. The left and centre panels differ only in the dynamic range of the pixel values: the density map shown on the left saturates at high values while the map in the centre saturates at much lower density levels. Traced with RR Lyrae, the Clouds do not appear very round. In the MS coordinate system, the LMC is stretched in the North–South direction, while the SMC seems to be vertically squashed. This stretching can also be seen in Fig. 2 which shows the raw star counts in the MB coordinates.

In both panels, a narrow and long structure linking the SMC and the LMC is obvious. This 'bridge' connects the Eastern side of the SMC and the Southern edge of the LMC. Its width roughly matches the extent of the SMC. The right panel of the figure shows

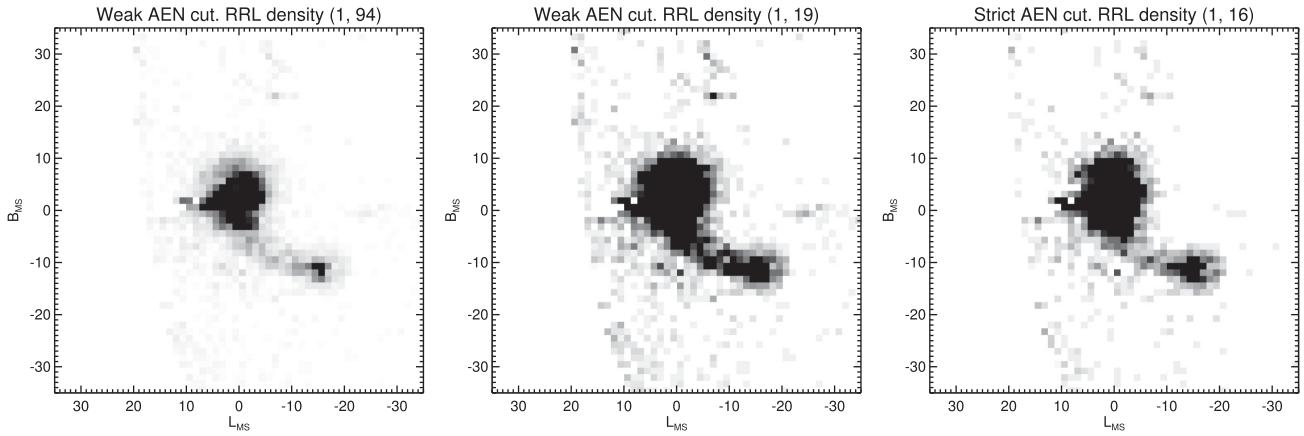

Figure 8. Density of the RR Lyrae candidate stars in $70^\circ \times 70^\circ$ area centred on the LMC in the MS coordinate system. Pixels are $1\overset{\circ}{.}25$ on a side. The pixel values corresponding to black and white are given in brackets in the title of each panel. Left and centre: ∼23 000 stars selected using (amongst others) a $\log_{10}(\mathrm{AEN}) < 0.25$ cut (see Fig. 4 for details). The difference between the two panels is only in the maps' dynamic range as indicated in the panel titles. Both Clouds are clearly visible as well as a bridge connecting them, with a cross-section roughly matching that of the SMC. Right: density map of the 10501 RR Lyrae candidates selected using a stricter $\log_{10}(\mathrm{AEN}) < -0.2$ cut. Here, most of the artefacts related to the cross-match visible in the centre panel disappear, albeit at the expense of the noticeable reduction in the sample size.

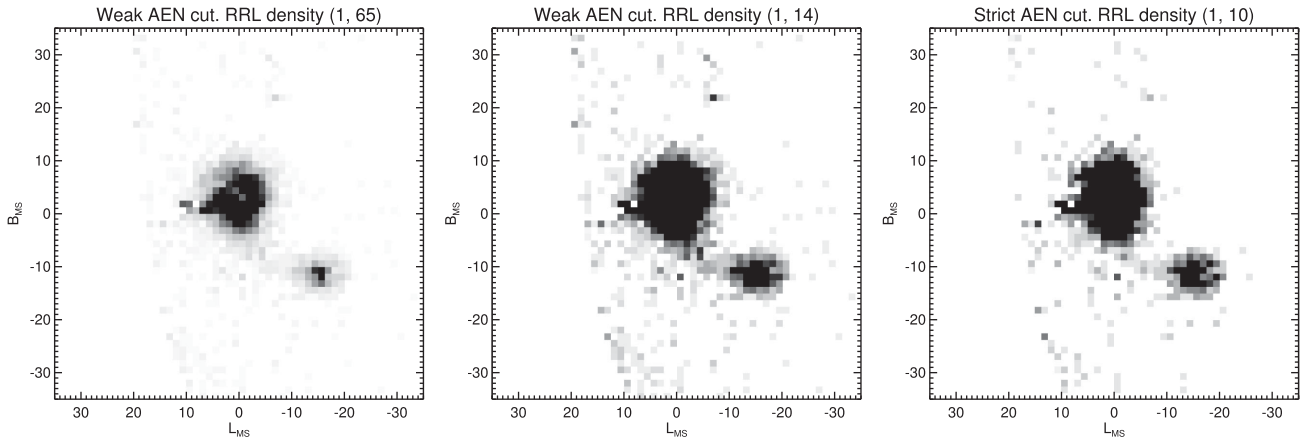

Figure 9. Same as Fig. 8 but with an $\mathrm{Amp} > -0.65$ cut.

the density of RR Lyrae candidates selected using a stricter cut on AEN. While the bridge is clearly less prominent in the right panel, its width and length remain largely unchanged. A version of the RR Lyrae density map is shown in Fig. 9. Here, the cut on the variability amplitude is stricter, i.e. $\mathrm{Amp} > -0.65$, which allows us to relax the cut on astrometric excess noise, i.e. $\log_{10}(\mathrm{AEN}) < 0.3$ (left and centre panels; also see Section 3 for the discussion of the effects of different selection criteria). Finally, the right panel of the figure shows a density map of the 'double-distilled' sample of RR Lyrae candidates: with $\mathrm{Amp} > -0.65$ and $\log_{10}(\mathrm{AEN}) < -0.2$. Reassuringly, the bridge remains visible, regardless of the level of 'cleaning' applied. However, the number of stars in the bridge drops significantly with stricter cuts. Importantly, as the completeness and the purity varies, across all six panels of the Figs 8 and 9 combined, the shape of the GSDR1 RR Lyrae distribution looks consistent.

Comparing the RR Lyrae density maps to the distribution of artefacts shown in the rightmost panel of Fig. 5, we note that the bridge does not appear to follow any particular spurious over-density and its borders are not coincident with boundaries of the cross-match affected areas. However, the pronounced decrease in the bridge number counts on moving from the middle panel of Fig. 8 to the right panel of Fig. 9 may nonetheless imply that while the shape of the bridge is robust, its density levels are affected by spurious variables. Comparing to the bottom panel of Fig. 1, it is clear that none of the features in the RR Lyrae density map are coincident with the details of the Galactic dust distribution either. Therefore, we judge the RR Lyrae map not to be seriously affected by the effects of interstellar extinction. Overall, we conclude that the RR Lyrae bridge seen between the two Clouds is a genuine stellar structure.

We investigate the properties of the GSDR1 RR Lyrae bridge using the MB coordinate system defined above. In these coordinates, the RR Lyrae bridge runs parallel to the equator and is limited to $-7^\circ < Y_{\mathrm{MB}} < -1^\circ$. To obtain the centre and the width of the RR Lyrae distribution in each bin of X_{MB}, we fit a model which includes a linear foreground/background and a Gaussian for the stream's signal. The measured centroid and the width values are reported in Table 1. The top panel of Fig. 10 gives the density of RR Lyrae selected using the 'weak' version of the cuts presented in equation (3). The middle panel of the figure shows the background-subtracted number density profile along the bridge (black histogram). For comparison, grey (red) histogram shows the number density profile obtained using the sample of GSDR1 RR Lyrae obtained with $\mathrm{Amp} > -0.65$ and $\log_{10}(\mathrm{AEN}) < 0.3$ ($\log_{10}(\mathrm{AEN}) < -0.2$) cuts. Regardless of which set of the RR Lyrae

Table 1. Properties of the RR Lyrae bridge.

$X_{\rm MB}$	−5.6	−6.9	−8.1	−9.4	−10.6	−11.9	−13.1	−14.4	−15.6	−16.9	−18.1
$Y_{\rm MB}$	−2.2	−4.1	−5.3	−3.9	−4.6	−4.3	−4.4	−3.2	−2.5	−2.1	−1.2
σ_Y	1.7	2.1	1.4	2.3	1.1	1.7	1.7	2.1	2.2	1.1	1.6

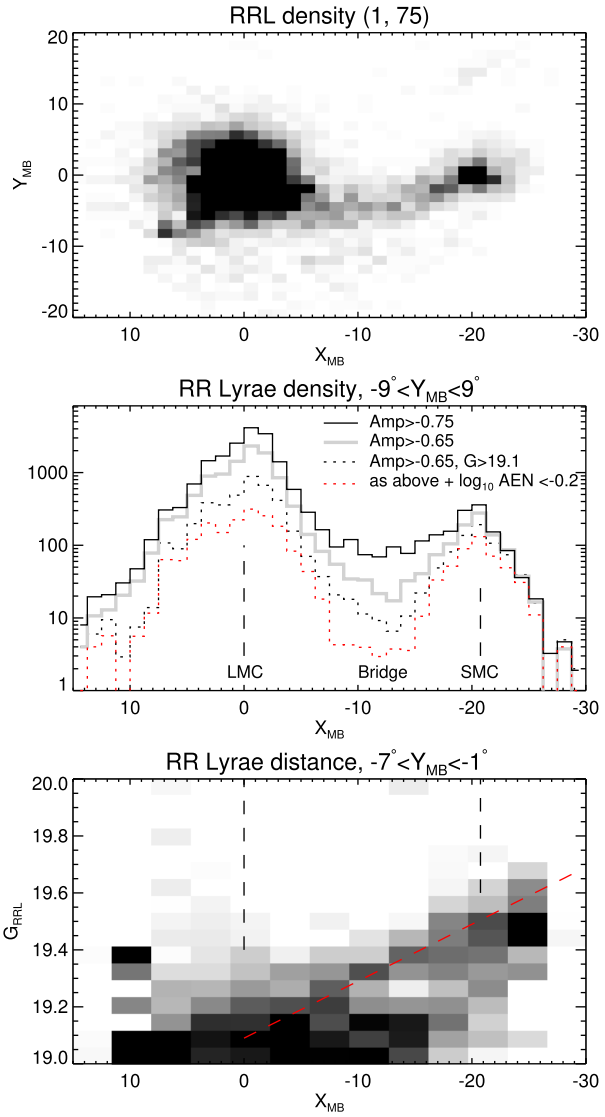

Figure 10. Top: density of the *Gaia* RR Lyrae candidates in the MB coordinate system in which both the LMC and the SMC lie on the equator. The pixel size is 1.°25 on a side. Middle: density of the RR Lyrae candidate stars along the MB equator. A foreground/background model (linear along MB latitude $Y_{\rm MB}$ and different for each $X_{\rm MB}$) is subtracted. The inset explains the cuts applied for each of the histograms. Bottom: variation of the apparent magnitude of the RR Lyrae along the bridge. For these RR Lyrae, a stricter cut on variability amplitude was applied, namely Amp > -0.65. Between the LMC and the SMC, two structures at distinct distances are visible: one at the distance of the LMC, i.e. at $G \sim 19$ and one connecting the LMC and the SMC (at $G \sim 19.5$). Red dashed line gives the approximate behaviour $G = 19.02 - 0.2X_{\rm MB}$ of the more distant of the two RR Lyrae structures.

selection criteria is used, the bridge density profile appears to have a depletion around the mid-point, i.e. at $X_{\rm MB} \sim -12^\circ$. The simplest interpretation of this behaviour is that the objects in this area of the sky come from two groups of stars, one around the LMC and one emanating from the SMC, each with a negative density gradient away from each Cloud. This could also explain the change in the curvature of the bridge at around $X_{\rm MB} \sim -10^\circ$.

Given that the LMC and the SMC are offset with respect to each other along the line of sight, it should be possible to test the above idea. To that end, the lower panel of Fig. 10 shows the apparent magnitude distribution of the Amp > -0.65 and $\log_{10}$(AEN) < 0.3 RR Lyrae with $-7^\circ < Y_{\rm MB} < -1^\circ$ as a function of the MB longitude $X_{\rm MB}$. As expected, the bulk of the LMC's RR Lyrae are around $G \sim 19$ while those belonging to the SMC aggregate in the vicinity of $(X_{\rm MB}, G) = (-20.^\circ75, 19.5)$. Between the LMC and the SMC, i.e. $X_{\rm MB} = 0^\circ$ and $X_{\rm MB} = -20.^\circ75$, there appear to be two distinct sequences. First, the more pronounced, at constant $G = 19$ extends from $X_{\rm MB} = 0^\circ$ to at least $X_{\rm MB} \sim -15^\circ$, or possibly further. Additionally, there is a clear second, albeit seemingly less populated, sequence which appears to connect the SMC and the LMC. Therefore, at a number of locations along the bridge there are two stellar over-densities, one at the distance of the LMC, and one travelling from the SMC towards the LMC. In the figure, the debris around the LMC's nominal distance appears to be more numerous at each sightline through the bridge. However, this apparent line-of-sight distribution is misleading as the RR Lyrae sample completeness is a strong function of the G magnitude. Given that at the SMC's distance, the completeness is at least three times lower, it is entirely possible that the bridge contains as much distant (i.e. at distances between the LMC and the SMC) debris as there is at the LMC's distance. In the future (and certainly with *Gaia* DR2), it should be possible to disentangle the bridge debris in 3D. However, already with the current data it seems likely that the inflection point in the bridge centroid at around $X_{\rm MB} = -10^\circ$ is due to the change in the ratio of the debris groups at different distances.

Using the background-subtracted density profile discussed above, it is feasible to estimate the total number of RR Lyrae in the bridge. However, because the GSDR1 RR Lyrae completeness is a strong function of apparent magnitude, the complex 3D structure of the bridge also needs to be taken into account. We define the bridge extent as that limited by $-15^\circ < X_{\rm MB} < -10^\circ$. This is motivated by the line-of-sight map shown in the lower panel of Fig. 10. Outside of this $X_{\rm MB}$ range, the RR Lyrae sample is dominated by stars that are currently still (likely) part of the LMC or the SMC. For the calculation below, we assume that the LMC provided the bulk of stars with $G < 19.1$ and the stars with $G > 19.1$ are mostly from the SMC (note, however, the discussion below and in Section 5.1). There are 75 RR Lyrae with $18.7 < G < 19.1$, which given the ∼30 per cent completeness (see Section 3.3) would translate into 250 RR Lyrae stars from the LMC – or at distances consistent with that of the LMC – in this region. There are 40 RR Lyrae with $G > 19.1$, all of which we tentatively assign to the SMC. As the dashed black histogram in the middle panel of Fig. 10 demonstrates, the density of these stars as a function of $X_{\rm MB}$ is reasonably flat within the bridge range specified above. Assuming the variation in completeness from 0.3 at $G = 19$ to 0.11 at 19.5 and assuming the distance to the SMC tidal tail goes like $G = 19.02 - 0.2X_{\rm MB}$ (shown as the red dashed diagonal line in the bottom panel of Fig. 10), we estimate a total of 240 RR Lyrae that could have been pulled out from the SMC. Note that the number of the RR Lyrae with $G > 19.1$ detected in this area drops to 14 if a

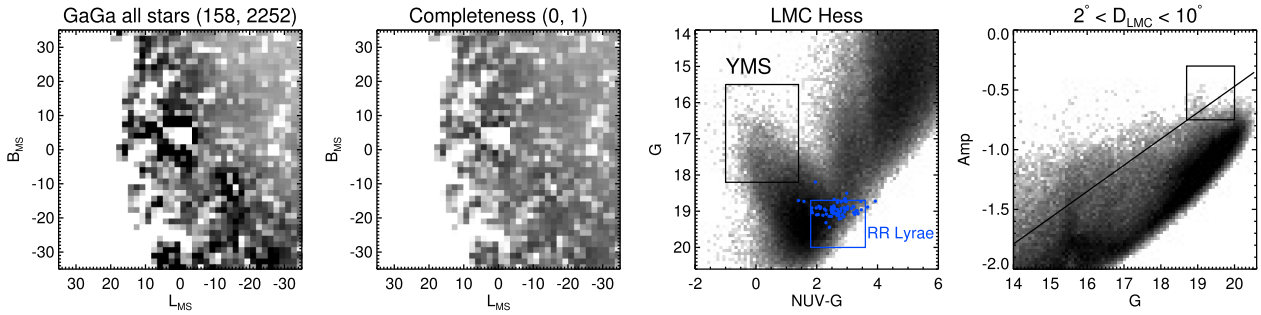

Figure 11. Selecting Magellanic RR Lyrae and YMS stars with GaGa = *Gaia*+*GALEX*. First panel: density map of stars with both *Gaia* and *GALEX* detections. The pixel size is 1.°667 on a side. Second panel: completeness map of GaGa. Third panel: logarithm of density in the colour–magnitude space (Hess diagram) spanned by G and $NUV - G$ for stars with $2^\circ < D_{\rm LMC} < 10^\circ$. Two selection boxes are shown: one aimed at identifying Magellanic RR Lyrae stars (blue) and one for YMS stars (black). Fourth panel: logarithm of density of GaGa sources in the space spanned by Amp and G for a region around the LMC. The LMC RR Lyrae are clearly identified in the designated selection box. Note that we use a slightly different cut on astrometric excess noise, i.e. $\log_{10}(\mathrm{AEN}) < -0.1$.

strict cut on astrometric excess noise ($\log_{10}(\mathrm{AEN}) < -0.2$) is applied. This would imply that at most 70 RR Lyrae may exist here. Worse still, we have not corrected any of these numbers for contamination, which we assumed to be (at least approximately) taken care of by the subtraction of the background model. Of course, if this region is overdense in spurious variables, the contamination will be far from zero. Also note that the above differentiation of the RR Lyrae into those belonging to the LMC and the SMC solely based on their apparent magnitude is very simplistic. This classification should be carried out using the actual distances to these stars.

The above discussion also glosses over some important details of the LMC's structure (such as line-of-sight distance gradients) as well as the details of its interaction with the SMC (i.e. the stars consistent with the LMC's distance could in fact be the SMC debris stripped much earlier). The latter will be dealt with in Section 5.1. With regard to the former, let us point out that a pronounced distance gradient has been measured across the LMC's disc (see e.g. Mackey et al. 2016). This gradient is positive in the direction of the decreasing $X_{\rm MB}$. This necessarily implies that at least some of the debris with $G > 19.1$, are in fact part of the LMC. It is not clear, however, how far this LMC population can stretch. Saha et al. (2010) find evidence for the LMC stars at angular separations of $\sim$15°. According to Mackey et al. (2016), on the other side of the dwarf, the disc is perturbed into a stream-like structure visible at $X_{\rm MB} \sim 13.^\circ5$. If a counterpart to the Mackey et al. (2016) 'stream' exists, then many of the distant RR Lyrae stars in the bridge at $X_{\rm MB} \sim -10^\circ$ (and maybe as far as $X_{\rm MB} \sim -15^\circ$) are from the LMC's disc. We investigate this possibility further with simulations in Section 5.1. This leaves the nature of the portion of the RR Lyrae with constant $G \sim 19$ and $10^\circ > X_{\rm MB} > -15^\circ$, seen as a dark horizontal bar in the bottom panel of Fig. 10, rather unclear. Curiously, Belokurov & Koposov (2016) report a very similar structure (dubbed S1), i.e. a large group of LMC stars in a fixed narrow distance range, on the opposite side of the LMC. The top left panel of their fig. 18 clearly shows that S1 stars do not follow the disc's distance gradient. While the distance modulus range of S1 is very restricted, it spans a wide range of angles on the sky. This mostly flat, two-dimensional structure resembles the distribution of the RR Lyrae on the Cloud's side facing the SMC and is suggestive of a disc origin.

4.2 The *GALEX* litmus test and the Young Main Sequence bridge

So far, for the RR Lyrae selection we have relied solely on the photometry provided as part of the GSDR1. While measures of all sorts have been taken to guard against contamination, at the moment it is impossible to gauge with certainty the amount of spurious variability supplied by the cross-match failures. However, there exists an additional test which can help us to establish whether the discovered bridge is genuinely composed of pulsating horizontal branch stars. RR Lyrae are hot helium burning stars and as such occupy a narrow range of broad-band colour. Unfortunately, no deep optical survey provides a wide-area coverage of the entire Magellanic system. Nonetheless, it turns out that the brightest of the Magellanic RR Lyrae are seen by the *GALEX* space telescope.

Fig. 11 gives the *GALEX* DR7 (GR7, Bianchi, Conti & Shiao 2014) coverage of the 70° × 70° region around ($L_{\rm MS}$, $B_{\rm MS}$) = (0°, 0°). As can be seen in the leftmost panel of the figure, the *GALEX* view of the Clouds is very patchy. However, as shown in the second panel of the figure, most of the pixels around the LMC and the SMC have non-zero completeness. The third panel of the figure shows the Hess diagram (density of sources in colour–magnitude space) for the LMC sources measured by both *Gaia* and the *GALEX* AIS (the GaGa sample). As is clear from the distribution of the previously identified RR Lyrae stars (blue), the brightest of these are indeed present in GaGa and, as expected, occupy a narrow range of $NUV - G$ colour. The rightmost panel of the figure displays the familiar variability–magnitude diagram for the GaGa stars within 10° radius from the LMC. Within the designated RR Lyrae box, an overdensity of objects is visible. These stars are not only identified as variable by *Gaia*, but also possess the $NUV - G$ colour consistent with that of the RR Lyrae. The latter is true even though no colour cuts were applied to select stars included in the diagram. This is because at the magnitudes as faint as $G > 18.5$ the *GALEX* selection effects are strong, and only stars with noticeable UV flux would be detected by *GALEX* (as seen in the third panel of the figure). Nonetheless, the selection of likely GaGa RR Lyrae candidates can be tightened if a colour cut – shown as the blue box in the third panel of the figure – is applied.

The left panel of Fig. 12 shows the distribution of the GaGa RR Lyrae candidates (blue points) in the MS coordinate system. Also shown are the contours of the GSDR1 RR Lyrae density (black) corresponding to the selection shown in the left and centre panels of Fig. 8. The completeness of the GaGa RR Lyrae sample is truly minute, but its purity – thanks to the additional colour cut – is likely very high. The central part of the LMC is missing from the GR7, and hence there is a large hole in the distribution of blue points. At large angular distances from the LMC, two prominent extensions of the GaGa RR Lyrae are traceable. The first one is directly to the North from the LMC at $10^\circ < B_{\rm MS} < 20^\circ$. This Northern RR Lyrae

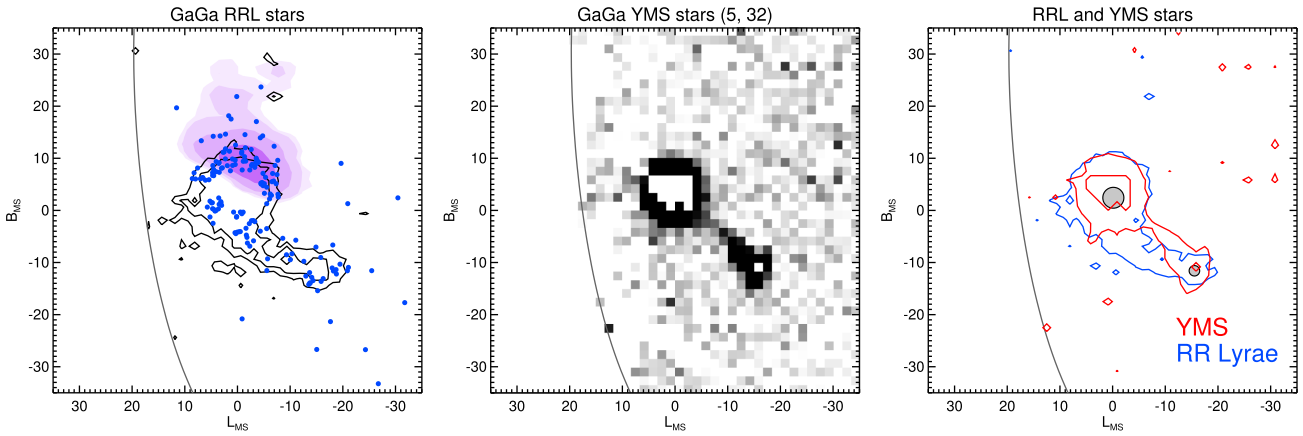

Figure 12. Left: positions of 167 GaGa RR Lyrae candidates. Contours show the density of *Gaia* DR1 RR Lyrae candidates. Outside of the main LMC body, there are two clear overdensities of the GaGa RR Lyrae. First, the one between the LMC and the SMC, corresponding to the bridge reported in Fig. 8. Additionally, there is a plume of GaGa RR Lyrae which extends to the North of the LMC in agreement with BHB detections (shown as purple density contours) reported in Belokurov & Koposov (2016). Centre: density of ∼45 000 YMS candidates in GaGa. Note that the YMS stars trace a different, much narrower bridge, clearly offset from the RR Lyrae tail. Right: comparison of the density distributions of the *Gaia* RR Lyrae candidates (blue) and GaGa YMS candidates (red).

plume overlaps with at least two recently discovered LMC substructures. First, a section of the LMC's disc appears to be pulled in the direction of increasing $B_{\rm MS}$ as reported by Mackey et al. (2016). Additionally, a large tail of BHBs has been detected by Belokurov & Koposov (2016), stretching as far as $B_{\rm MS} \sim 25^\circ$ (S1 stream; e.g. their fig. 6). The BHB density contours corresponding to the edge of the LMC disc and the S1 structure are shown in purple. The second plume of GaGa RR Lyrae is coincident with the GSDR1 bridge presented earlier and reaches from the LMC to the SMC. Note that the SMC itself is not very prominent, due to the drop in the GR7 AIS completeness at faint magnitudes.

The Hess diagram shown in the third panel of Fig. 11 also reveals a well-populated YMS, seen as a cloud of stars with $NUV - G < 2$ and $G < 19$. Taking advantage of this strong CMD feature and of the GaGa wide coverage of the Clouds, we select YMS candidates using the CMD box shown in black (without any cuts related to the stellar variability as seen by *Gaia*). The centre panel of Fig. 12 displays the density map of the GaGa YMS candidate stars. Once again, the central parts of the LMC and the SMC are missing due to the GR7 footprint irregularities. However, the outer portions of the discs of both Clouds can be seen rather clearly. Moreover, a narrow tongue of YMS stars appears to stick out of the SMC and reach some 10° across to the LMC. As the right panel of the figure clearly demonstrates, the RR Lyrae and the YMS bridges are not coincident and follow distinct paths between the Clouds.

Fig. 13 presents the view of the YMS bridge in the MB coordinate system. The top panel of the figure shows that the YMS bridge is a very narrow structure, which is nearly perfectly aligned with the MB equator. We use a model identical to that described in Section 4.1 to extract the centroids and the widths of the YMS bridge as a function of $X_{\rm MB}$ and report these in Table 2. The bottom panel of the figure shows the density profile of the YMS bridge with background/foreground contribution subtracted. The density along the bridge drops somewhat in the periphery of the LMC, but otherwise is moderately flat with the exception of a large excess of YMS stars in the Wing, i.e. on the side of the SMC facing the LMC, at $-20^\circ < X_{\rm MB} < -15^\circ$.

Fig. 14 compares the behaviour of the RR Lyrae and the YMS bridges as a function of the position on the sky. Throughout most of

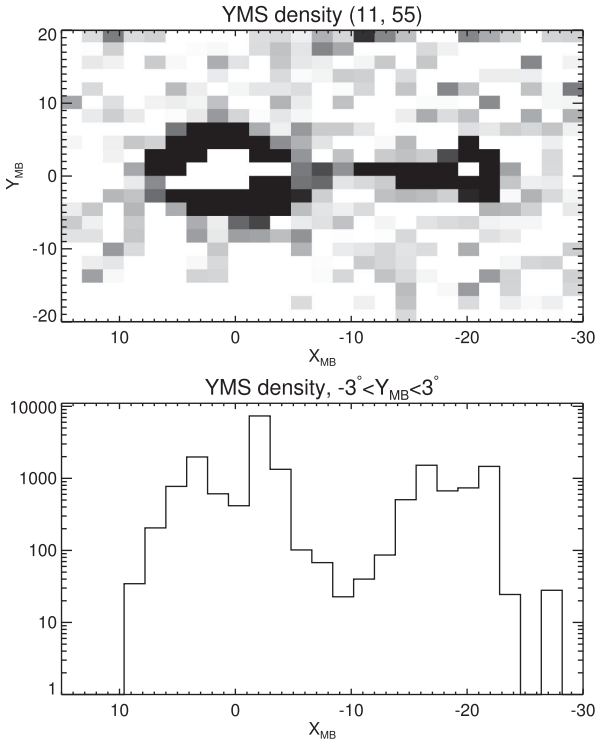

Figure 13. Top: density of the GaGa YMS candidates in the MB coordinate system in which both the LMC and the SMC lie on the equator. The pixel size is 1.°8 on a side. Bottom: density of the GaGa YMS candidate stars along the MB equator. A foreground/background model (linear along MB latitude $Y_{\rm MB}$ and different for each $X_{\rm MB}$) is subtracted.

Table 2. Properties of the YMS bridge.

$X_{\rm MB}$	−7.5	−9.3	−11.1	−12.9	−14.7	−16.5	−18.3
$Y_{\rm MB}$	0.0	1.3	0.2	0.9	0.3	0.1	−0.2
σ_Y	0.5	1.1	0.4	1.0	0.9	0.9	1.0

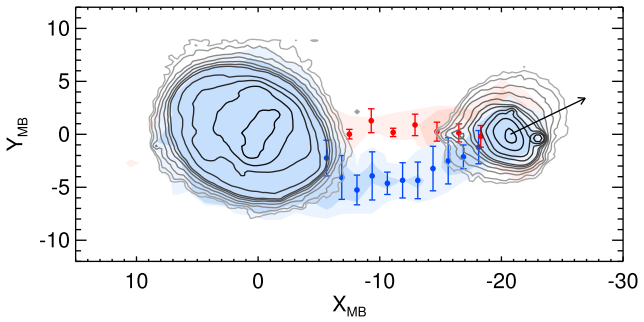

Figure 14. Comparison between the RR Lyrae (blue) and the YMS (red) bridges. The filled circles (error bars) mark the centroids (widths) of each structure as extracted by the model (also see Tables 1 and 2). The two structures are clearly offset on the sky at most X_{MB} longitudes between the Clouds. However, they appear to connect to the SMC at approximately the same location on the east side of the dwarf. The contours give the all-star density distribution. The black arrow indicates the relative proper motion of the SMC with respect to the LMC. The YMS bridge connects to the Wing, while the RR Lyrae bridge connects to the southern portion of the S-shape. The conclusion is therefore inescapable that at least the portion of the RR Lyrae bridge closest to the SMC represents the dwarf's trailing tidal tail.

the LMC–SMC span, the two bridges are clearly offset from each other, with the largest angular separation being of the order of $\sim 5^\circ$. At the distance of the bridge, this angular separation corresponds to $\sim$5 kpc. Importantly, both connect to the SMC at approximately the same location on the eastern side of the dwarf. Note also the striking match between the all-star-count distribution (shown as contours) and the YMS/RR Lyrae bridge density. This figure demonstrates rather clearly that the RR Lyrae bridge is the continuation of the lower part of the S-shape discussed in Section 2.3. We therefore conclude that the portion of the RR Lyrae bridge closest to the SMC is the extension of the dwarf's trailing arm. Given the line-of-sight distribution discussed in Section 4.1, at $X_{MB} > -15^\circ$, the bridge may be dominated by the LMC's stars. However we cannot rule out that some of the SMC's tidal debris reaches as far as the Large Cloud or beyond.

4.3 The H I bridge

Fig. 15 shows the density map of neutral hydrogen in and around the Clouds, based on the data from Galactic All-Sky Survey (GASS; see Kalberla & Haud 2015).[3] This represents the column density of H I gas with heliocentric velocities 100 km s^{-1} $< V <$ 300 km s^{-1} – a range that encompasses the bulk of H I in the Magellanic system. As the figure illustrates, the regions of the highest gas density are coincident with the LMC and the SMC (red contours). There is plenty of gas in between the Clouds as well as trailing behind them (the MS), albeit at lower density. Besides the Clouds themselves, the highest concentration of H I appears to be in a narrow ridge-line structure, connecting the SMC and the LMC, known as the MB (mostly yellow contours).

It is obvious from the figure that the GSDR1 RR Lyrae bridge is not coincident with the main H I ridge of the inter-Cloud H I reservoir. Instead, it is offset South-East, or, in other words, is leading the gaseous bridge. Curiously, the Southern edge of the H I distribution matches tightly the edge of the RR Lyrae bridge. The YMS bridge, on the other hand, appears to sit almost exactly on

[3] https://www.astro.uni-bonn.de/hisurvey/gass/.

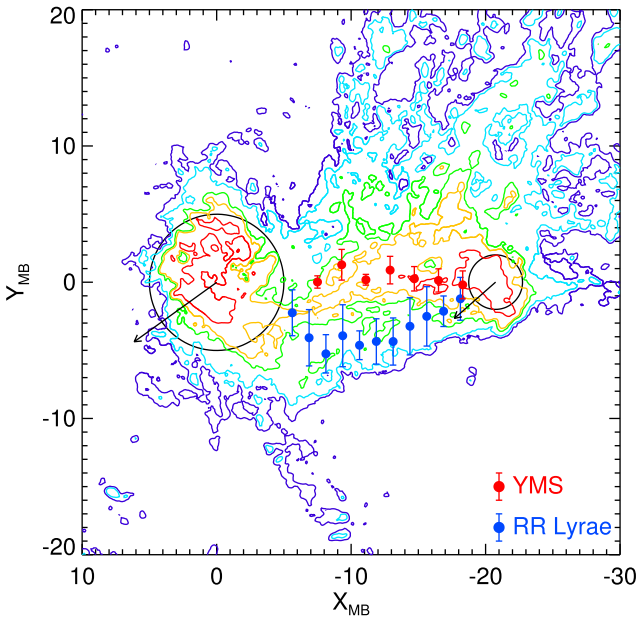

Figure 15. The three Magellanic bridges in the MB coordinate system. Contours give the density of the H I gas in the velocity range $100 < V_{LOS}$(km s^{-1} < 300). Red, yellow, green, blue and purple contours correspond to gas column density of (12.02, 3.18, 1.80, 0.46, 0.16) $\times$ 10^{-20} cm^{-2}. Blue (red) filled circles with error bars give the evolution of the centroid and the width of the RR Lyrae (YMS) bridge as a function of the MB coordinates. Blue filled circles with error bars show the evolution of the centroid and the width of the RR Lyrae bridge. The LMC and the SMC are shown as large circles. Arrows give the proper motion vectors of the Clouds from Kallivayalil et al. (2013) in the MB coordinate system.

the spur of the H I from the SMC. The obvious conclusion from the distribution of the young and the old stars in comparison to the neutral hydrogen is that the YMS stars have formed in the gaseous bridge which was stripped together with the RR Lyrae, but was pushed back (with respect to the Clouds proper motion) by the ram pressure exerted by the gaseous halo of the Galaxy. Also shown here are the arrows corresponding to the proper motion vectors of the Clouds as measured by Kallivayalil et al. (2013). In Section 5.5 we will use the offset between the young and old stars to estimate the gas density of the Milky Way halo.

5 DISCUSSION AND CONCLUSIONS

5.1 Comparison to the simulations

In this section we look to numerical simulations of the LMC and SMC interaction in an attempt to interpret the RR Lyrae candidate distribution presented above. In particular, we seek to find answers to the following questions. Does the orientation of the RR Lyrae bridge on the sky agree with the recently measured proper motions of the Clouds? What could be responsible for an inflection of the SMC's trailing tail at $X_{MB} \sim -10^\circ$? What is the relative contribution of each Cloud to the bridge density? Here, we consider three separate simulation setups: two which model the debris from the SMC in the presence of the LMC, and one which only follows the LMC on its orbit around the Milky Way. To produce realistically looking SMC debris as it disrupts in the presence of the LMC, we use the modified Lagrange cloud stripping technique of Gibbons et al. (2014).

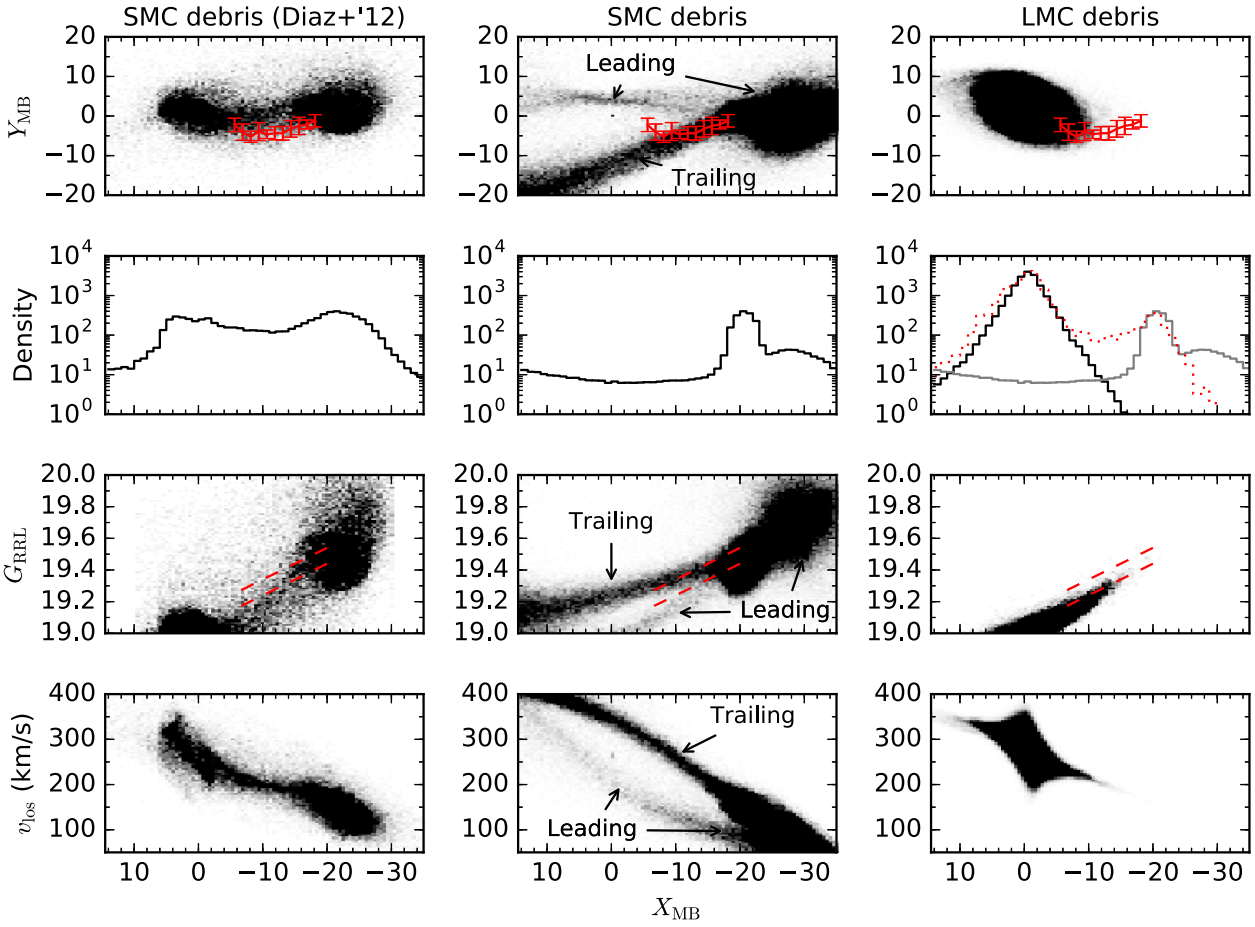

Figure 16. Debris from simulations of the SMC/LMC infall. The first column shows the debris from an SMC disruption similar to that in Diaz & Bekki (2012), the second column shows the SMC debris from a large number of simulations required to match the position of the bridge on the sky, the third column shows the LMC debris from Mackey et al. (2016). The rows show different observables of the debris: debris on the sky in MB coordinates, density of the debris along $X_{\rm MB}$, the G-band magnitude of the debris, and the line-of-sight velocity of the debris. In the top row, we show the position of the old stellar bridge as a red line with error bars. In the third row, we show the observed distance gradient along the bridge with dashed red lines. Since the setup in Diaz & Bekki (2012) was designed to match the H I bridge, the stars are above the old stellar bridge on the sky. The SMC debris shown in the middle column was required to match the old stellar bridge and as a result is a better fit. The debris has broadly the same distance gradient as observed although there is a large spread. The LMC debris in the right column shows that the tidally disrupting LMC disc can also provide a contribution in the region of the old stellar bridge. Note for the density in the LMC setup, we also show the density for the SMC setup (grey histogram), as well as the observed density from Fig. 10 (red dotted histogram). Given that the simulated LMC density does not show any flattening, the observed flattening may be due to the SMC debris.

For the first simulation, we follow the setup of Diaz & Bekki (2012) with an LMC represented by a Plummer sphere with a mass of 10^{10} $M_\odot$ and a scale radius of 3 kpc while the SMC is modelled as a 3×10^9 $M_\odot$ Plummer sphere with a scale radius of 2 kpc. The Milky Way is modelled using a three-component potential made up of a Miyamoto–Nagai disc, a Hernquist sphere bulge, and an NFW halo (see Diaz & Bekki 2012, for more details). The SMC and LMC are rewound from the final positions given in Diaz & Bekki (2012) for 3.37 Gyr and then evolved to the present day. Material is stripped from the SMC during its pericentres around the LMC with a rate given by a Gaussian with a dispersion of 50 Myr. This debris is shown in the left column of Fig. 16 where the rows show the debris on the sky in MB coordinates, the density of the debris along $X_{\rm MB}$, the G-band magnitude of the debris, and the line-of-sight velocity of the debris. Diaz & Bekki (2012) identified this particular combination of parameters as it reproduced best the H I features of the MS and MB. As a result, it is not surprising that the debris goes straight from the SMC to the LMC, unlike the bridge seen in RR Lyrae (top left panel of Fig. 16). The distance gradient of this debris also seems somewhat off with respect to what is observed since it quickly reaches a similar distance as the LMC. This is because the debris from the SMC is accreted on to the LMC in this setup. While this simulation provides only an approximate match to the RR Lyrae bridge, it shows that it is possible for SMC debris to attach on to the LMC. Thus, it is in principle possible that a different setup could provide a better match to the RR Lyrae observation presented here while also connecting to the LMC and hence following the upturn in the bridge seen near the LMC. Note that there exists important – albeit circumstantial – evidence as to the existence of the SMC stellar debris inside the LMC (see e.g. Olsen et al. 2011), which would superficially support the idea that the RR Lyrae bridge extends uninterrupted all the way from the Small to the Large Cloud.

In the second simulation where we study the SMC debris, we use a much more massive LMC modelled as a Hernquist sphere with a mass of 2.5×10^{11} $M_\odot$ and a scale radius of 25 kpc. This heavy LMC is in better agreement with the results of e.g. Besla et al. (2010) and Peñarrubia et al. (2016) as well as the constraint on the mass

enclosed within 8.7 kpc from van der Marel & Kallivayalil (2014). For the SMC we use a 2×10^8 $M_\odot$ Plummer sphere with a scale radius of 1 kpc. The Milky Way is modelled as a three-component potential `MWPotential2014` from Bovy (2015). Using the updated proper motion measurements for the LMC and SMC from Kallivayalil et al. (2013), the line-of-sight velocities from van der Marel et al. (2002) and Harris & Zaritsky (2006) for the LMC and SMC, respectively, and the distances from Pietrzyński et al. (2013) and Graczyk et al. (2014), respectively, we sample the position and velocity of the LMC and SMC. For each sampling, we rewind the LMC and SMC for 3 Gyr, and then simulate the disruption of the SMC. For each disruption, we construct a χ^2 based on location of the bridge on the sky and the bridge in distance and choose only the simulations with $\chi^2/\mathrm{d.o.f.} < 1$. From 1000 simulations, we find only 45 which satisfy the criteria suggesting that the location of the bridge can be used to place tighter constraints on the proper motion of the LMC and SMC. The combination of debris from these 45 simulations is shown in the middle column of Fig. 16. This debris roughly matches the bridge's shape on the sky although it does not display the turn-up seen in the data near the LMC. Instead, it streams past the LMC to the South East. While the trailing tail of the debris roughly matches the old stellar bridge, the leading tail of the SMC reaches apocentre with respect to the LMC and then heads back towards the LMC. Note that the leading and trailing tails have different positions on the sky (the trailing tail is below), different distances (the trailing tail is farther away), and different line-of-sight velocities (the trailing tail has a higher velocity). Also note that most of the stars in the leading tail of the SMC are to the West of the SMC and more distant, beyond the range RR Lyrae can be detected with GDR1. Furthermore, the segment of the leading tail which appears as a stream has very few stars compared to the trailing tail and thus may be too sparse to detect with GDR1. Deeper future surveys, including GDR2, should be able to detect the leading tail of the SMC. While beyond the scope of this work, we note that the precise track of the trailing and leading tail depends on the MW potential. Thus, future modelling efforts may be able to use the old stellar bridge to get a constraint on the MW halo.

We note that these simulations of the SMC debris neglect several important effects. First, we do not account for the dynamical friction of the SMC in the presence of the LMC. If dynamical friction were included, the SMC would have been farther away in the past and would have stripped less. As a result, the length of the streams in Fig. 16 can be reduced depending how effective dynamical friction is. Secondly, the Lagrange cloud stripping technique was not designed to correctly model the density along the stream with respect to the dwarf, rather it is designed to match the stream track in position and velocity. Thus, the peaky SMC density in the middle column of Fig. 16 should not be over-interpreted. As a test of the second set of simulations, especially given the small pericentres of the SMC with respect to the LMC, we have run several *N*-body simulations with GADGET-3 (similar to GADGET-2; Springel 2005). In these simulations, the LMC is modelled as a particle sourcing a Hernquist potential and the SMC is modelled as a live Plummer sphere with 10^5 particles. The pattern of debris looks almost identical showing that the Lagrange cloud stripping technique works well.

Finally, we have a simulation of the evolution of the LMC disc under the Galactic tides, identical to that in Mackey et al. (2016). Unlike the previous two setups, this simulation contains no SMC and thus neglects the perturbations that it can impart on the LMC (e.g. Besla et al. 2012, 2016). However, it does capture the response of the LMC to the Milky Way. This setup involves a live two-component *N*-body LMC (disc+dark matter) disrupting in the presence of a live three-component Milky Way (see Mackey et al. 2016, for more details). The stars from the LMC disc are shown in the rightmost column of Fig. 16. The LMC disc debris stretch out to the location of almost the entire bridge. In addition, the distance gradient matches the bridge. Thus, it is likely that some of the bridge, and perhaps the upturn near the LMC, is due to debris from the LMC. This is emphasized in the second row, third column panel of Fig. 16 where we show the density of the LMC (black histogram), the density of the SMC debris from the middle column (grey histogram) and the observed density of RR Lyrae from Fig. 10 (black histogram from second column). We see that the observed density matches the LMC quite well for $X_{\mathrm{MB}} < 7^\circ$, after which it flattens out. The flattening beyond $X_{\mathrm{MB}} > 7^\circ$ is likely due to SMC material. Note that the simulated density has been scaled to match the observed density peak near the LMC and SMC.

The simulations show that around the LMC, both the Large and the Small Cloud can naturally produce debris which is closely aligned with the RR Lyrae bridge on the sky and in distance (right two columns of Fig. 16). Fortunately, these debris have different line-of-sight velocity signatures with the SMC debris having a much higher velocity, $\sim$50 km s^{-1}, at the same X_{MB}. Thus, spectroscopic follow-up of the stars in the RR Lyrae bridge should allow us to test whether the debris is partly made up of SMC and LMC debris and if there is a transition between the two. Note that the entire bridge could also come from SMC debris which would require an upturn near the LMC. Although the models shown in the middle column of Fig. 10 do not show this behaviour, a larger search of the parameter space may uncover SMC debris somewhere between the first and second columns. The radial velocity signature of this debris would presumably connect smoothly from the SMC to the LMC and not exhibit two distinct populations.

Based on the analysis of the simulations presented above, we conclude that at least at $X_{\mathrm{MB}} < -10^\circ$, the SMC trailing tail contributes most of the material to the RR Lyrae bridge. Additionally, as explained in Diaz & Bekki (2012) and shown in Fig. 16, there exists a counterpart to the trailing arm: the SMC's leading arm, mostly on the opposite side of the Cloud, albeit it is not arranged as neatly as the trailing. Instead, it is bending away from the observer and around the SMC, thus appearing much shorter on the sky as well as extending further along the line of sight. While a segment of the leading tail looks stream-like, most of the stars in the leading tail are in the field of debris to the West of the SMC. Note that all simulations discussed so far predict some of the SMC tidal debris outside of the main area of the RR Lyrae bridge. Much of the stripped material appears to lead the LMC. How far it can be flung out is likely controlled by the size of the SMC's orbit.

5.2 The stellar outskirts of the LMC

The focus of this paper is on the tidal tails of the SMC, in particular the trailing arm, which – when traced with RR Lyrae – has the appearance of a bridge connecting the Small Cloud to the Large. In this section, we concentrate on the properties of the distribution of the RR Lyrae residing in and around the LMC.

The left panel of Fig. 17 shows the locations (in the MS coordinate frame) of individual RR Lyrae candidate stars selected using the strict version of the cuts presented in equation (3), both in Amp and $\log_{10}$(AEN). This sample is then divided into four groups based on the star's azimuthal angle (indicated with colour). We use the stars in the blue and black groups to model the LMC's radial density profile, but avoid the red group as it runs into the regions of low

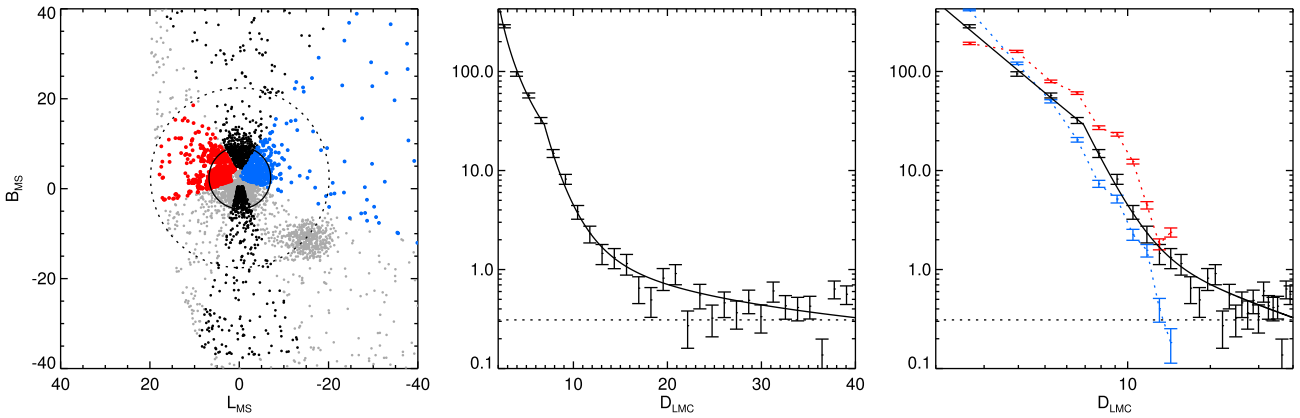

Figure 17. Left: distribution of ∼6000 *Gaia* DR1 RR Lyrae candidates in the MS coordinate system. These were selected with Amp > -0.65 and $\log(\mathrm{AEN}) < -0.2$ cuts. Sub-sets of stars coloured black and blue are used for the radial profile modelling reported in the centre and right panels. The solid circle marks the break radius of ∼7°, while the dotted circle simply shows the 20° boundary around the LMC. Centre and right: LMC RR Lyrae radial density profiles (black data points with error bars) and the maximum-likelihood BPL model (black line). Red and blue data points correspond to the leading and trailing parts of the LMC as shown in the left panel of the figure.

Galactic latitude as well as the grey group as it contains the SMC and its trailing tail (i.e. the bridge). The resulting radial density profile is shown in linear (logarithmic) scale in the middle (right) panel of the figure. Both panels demonstrate a clear change in the behaviour of the stellar density between 5° and 10° from the LMC's centre where the star-count rate drops noticeably. Also note that the RR Lyrae distribution extends as far as 20° from the centre of the LMC, if nor further.

Motivated by the behaviour of the LMC stellar density, we model the distribution of the candidate RR Lyrae stars with a broken power-law (BPL) (best-fitting solution shown as solid black curve). In a BPL model, the density distribution is described with a simple power law, but the power-law index is allowed to change at the break radius. The two power-law indices (inner and outer), the break radius and the (flat) background contribution are the free parameters of this model. Note that similar BPL models have been used successfully to describe the density profile of the Milky Way stellar halo (see e.g. Deason, Belokurov & Evans 2011; Sesar, Jurić & Ivezić 2011; Xue et al. 2015). The maximum-likelihood model of the 1D angular distribution of the RR Lyrae candidate stars in the black and blue groups places the break at the radius of $6.^{\circ}91 \pm 0.^{\circ}34$. The inner power-law index is 2.36 ± 0.08, while the outer power-law index is 5.8 ± 0.6. Deason et al. (2013) put forward a simple explanation of radial density breaks in the stellar haloes around Milky Way-like galaxies. In their picture, the breaks emerge if the stellar halo is dominated by a small number of massive progenitors that are accreted at reasonably early times.

Before we speculate as to the origin of the LMC's stellar halo, it is prudent to point out some of the drawbacks of the above modelling exercise, most notably, the assumption of spherical symmetry and the alignment of the disc and the halo. For example, if the centre of the LMC's disc is offset from the centre of the LMC's halo, the (mis-centred) radial density profile will acquire an artificial 'scale'. Furthermore, if beyond a certain radius the LMC's RR Lyrae distribution is flattened, the resulting number count profile may look 'broken'. There is some modest evidence for an elongation of the LMC as traced by the RR Lyrae as can be seen from the comparison of the black and blue lines in the right panel of Fig. 17. The black line gives the count for both black and blue points (thus indicating the average behaviour) in the left panel, but the blue line shows the properties of the blue points only. The blue profile is systematically above the black at small radii and sits below it at large angular distances. This may be because – in the MS system – the LMC is stretched vertically (or squashed horizontally).

Apart from the hints of a possible flattening, the RR Lyrae distribution also shows signs of asymmetry. This can be gleaned from the shape of the red line in Fig. 17 as compared to the overall profile (given in black). There appears to be a strong excess of RR Lyrae on the leading (with respect to its proper motion) side of the Cloud. This discovery agrees well with the most recent map of the Magellanic Mira stars presented in Deason et al. (2016) and discussed in more detail in Section 5.3.

The preliminary (due to the contaminated and largely incomplete RR Lyrae sample considered here) results can be compared to some of the recent attempts to measure the radial density profile of the LMC. The NOAO's Outer Limits Survey (OLS) obtained a large number of deep images of the LMC, in which the dwarf's Main Sequence population can be traced as far as ∼16° from its centre (see Saha et al. 2010). The MS counts in the OLS sample follow an exponential profile. However, the spectroscopically confirmed red giant branch (RGB) stars from the survey of Majewski et al. (2009) appear to have a break at the distance of ∼9° in the radial density profile. The RGBs consistent with the LMC population can be traced as far as ∼23° in agreement with the RR Lyrae distribution discussed above, albeit beyond the break, instead of steepening (as found here), their density profile flattens. Last year, Dark Energy Survey (DES) provided a deep and continuous view of a small portion of the LMC. The analysis of the DES data can be found in Balbinot et al. (2015) and Mackey et al. (2016). In agreement with Saha et al. (2010), Balbinot et al. (2015) find that the LMC stellar content is dominated by disc population with a truncation radius of ∼13 kpc. An independent examination of the DES data is reported in Mackey et al. (2016) who detect (i) pronounced East–West asymmetry in the Cloud's radial density profile as well as (ii) strong evidence for a very diffuse stellar component reaching beyond ∼20° from its centre. Both of these findings appear to be in excellent agreement with the results based on the GSDR1 RR Lyrae sample presented here. It, however, remains unclear what morphological component is responsible for the extended envelope of stars around the Large Cloud, the disc or the halo; where the interface between the two lies, and if the stellar halo exists what processes are responsible for its creation.

5.3 Comparison to Mira results

Deason et al. (2016) present a large number of candidate Mira stars in the vicinity of the Magellanic Clouds. This is a new sample of Mira constructed using a combination of *Gaia*, 2MASS and WISE colours as well as the *Gaia* variability statistic Amp and is estimated to have very low levels of contamination. Note that the sample of stellar tracers discussed in Deason et al. (2016) includes both Mira and SRVs shown in the second and the third panels of the top row of Fig. 3. Around the LMC, GSDR1 Mira stars are seen at reasonably large angular separations from the LMC, most prominently in the North, where they overlap with the 'stream' discovered by Mackey et al. (2016), in the South where they overlap with the beginning of the extension mapped by the RR Lyrae presented here. However, there is no indication of the Mira presence in the area covered by the RR Lyrae bridge, i.e. in between the Clouds. While this might be a reflection of the stellar population gradients in the SMC disc, this could actually be simply due to the very low stellar density in the bridge. This latter explanation is perhaps preferred as the Mira distribution in the SMC does show noticeable excess – see fig. 8 of Deason et al. (2016) – on the ends of the S-shape structure traced by the *Gaia*'s raw star counts, i.e. in the densest portions of the two tidal tails. Additionally, there are several Mira candidates in the East of the LMC (in the MS coordiante system), where they match the RR Lyrae excess discussed in Section 5.2.

The Mira stars in Deason et al. (2016) can also be traced to regions of the sky away from the Magellanic Clouds (see their fig. 11). In particular, some of the Mira identified *above* the Galactic plane at $l \sim -90^{\circ}$ could be associated with the SMC debris leading the Clouds. Searches for other stellar populations (like RR Lyrae stars) in the region of the predicted far-flung Magellanic debris will help confirm this result, and will further test models of the SMC/LMC infall.

5.4 RR Lyrae bridge in the OGLE IV observations

The OGLE IV's sample of the Magellanic RR Lyrae (see Soszyński et al. 2016) is both more complete and more pure compared to the one analysed here. The only advantage of the GSDR1 data is the unrestricted view of the both Clouds and the area between and around them. On inspection of the top panel of fig. 1 of Soszyński et al. (2016), it is evident that (i) OGLE IV has detected the RR Lyrae in the trailing arm of the SMC and (ii) it is impossible to interpret it as a narrow bridge-like structure using the OGLE data alone as it lies at the edge of the survey's footprint.

Further evidence as to the existence of the old tidal debris in the OGLE data can be found in Skowron et al. (2014). Their figs 11 and 13 show the distribution of the top RGB and the bottom RGB stars, corresponding to the intermediate and the old populations, respectively. While the intermediate-age stars (their fig. 11) do not trace any striking coherent structure in the inter-Cloud space, an uninterrupted bridge of old stars is obvious at the edge of the footprint (their fig. 13). Once again, unfortunately, the limited FoV does not allow an estimate of the actual width of the structure.

Most recently, Jacyszyn-Dobrzeniecka et al. (2016) presented a detailed study of the structure of the two Clouds and the area between them using a sub-sample of the OGLE IV RR Lyrae. After selecting only RRab pulsators and culling objects with uncertain light curve shape parameters from the original sample of ∼45 000 stars, the authors end up with ∼22 000 RR Lyrae. The results of this study can be summarized as follows. The RR Lyrae density distributions of the LMC and the SMC can be described with families of nested ellipsoids. In the LMC, Jacyszyn-Dobrzeniecka et al. (2016) detect a noticeable twist in the orientation of the major axes of the ellipsoids as a function of the distance away from the Cloud's centre, while the density field of the SMC appears much more regular and symmetric. Overall, no strong irregularities or asymmetries have been reported for either of the Clouds. With regard to the inter-Cloud space, the paper announces the presence of a small number of RR Lyrae, but nothing similar to a coherent structure discussed here.

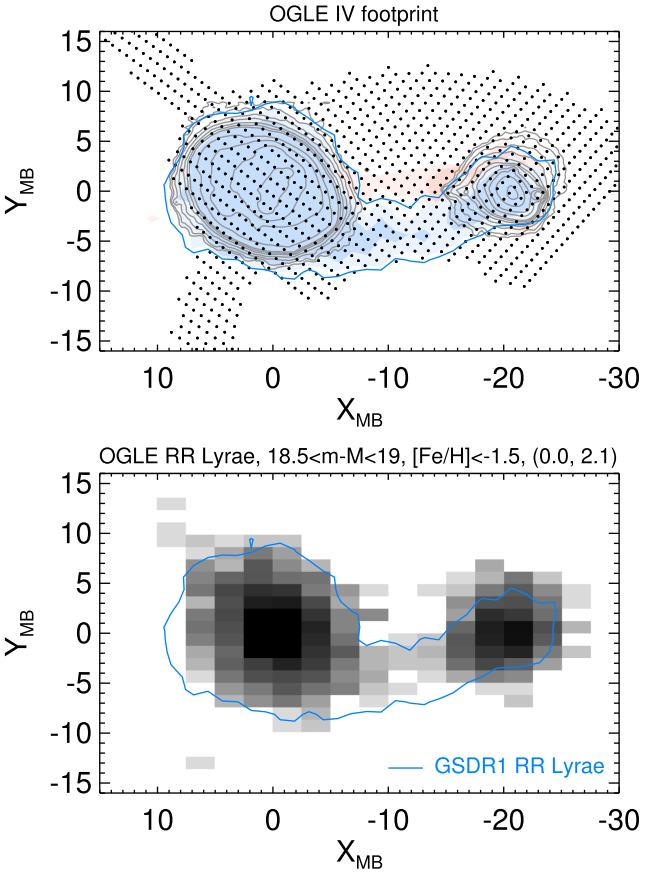

Figure 18. Top: OGLE IV footprint in MB coordinates. Locations of individual survey fields are marked with small black dots. Underlying are the density contours discussed earlier in the paper (see Fig. 14). Bottom: logarithm of the density of the OGLE IV RR Lyrae with $18.5 < m - M < 19$ and [Fe/H] < -1.5. A narrow structure connecting the two Clouds is clearly visible, matching the location, the extent and the breadth of the GSDR1 RR Lyrae bridge.

At a first glance, some of the conclusions reached in Jacyszyn-Dobrzeniecka et al. (2016) appear inconsistent with the substructure detections from the GSDR1 data. Around the LMC, this includes the Northern structure, i.e. overlapping with the Mackey et al. (2016) 'stream' and the S1 BHB/RR Lyrae stream (Belokurov & Koposov 2016), the Eastern excess of RR Lyrae (see Section 5.2 of this paper) as well as the Southern LMC extension, which could be responsible for as much as a half of the bridge we see in GSDR1. None of these entities seem to be confirmed with the OGLE IV data. However, the explanation for this seeming disagreement might be rather simple: all of the sub-structures mentioned above lie in the periphery of the Cloud, and thus do not fall within the OGLE IV's footprint shown in the top panel of Fig. 18. This is certainly true for the Northern and Eastern parts of the LMC. The OGLE IV coverage

of the Southern portion of the Cloud is broader, but even there, the structures reported here sit right at the edge of the footprint.

To compare the properties of the GSDR1 and OGLE IV RR Lyrae more directly, we build a map of the density distribution of a sub-sample of RRab pulsators from Soszyński et al. (2016). More precisely, we select RR Lyrae with well-determined light-curve shapes, i.e. those with errors on the ϕ_{31} and ϕ_{21} parameters smaller than 0.5. Additionally, we require the stars to lie at distances larger than that of the LMC but smaller than that of the SMC, i.e. $18.5 < m - M < 19$. Finally, we only plot metal-poor RR Lyrae, namely those with [Fe/H] < -1.5. The number of RR Lyrae satisfying all of the conditions above is approximately ∼3700 (which is approximately 1/5 of all RR Lyrae of ab type with good light curves within the designated distance range) and their density distribution is shown in the bottom panel of Fig. 18. According to Jacyszyn-Dobrzeniecka et al. (2016), the OGLE IV RR Lyrae cover a broad range of MB latitudes $Y_{\rm MB}$. However, as clear from the figure, the metal-poor subsample traces exactly the same narrow structure mapped out by the GSDR1 RR Lyrae candidates (also see Skowron et al. (2016) for the detailed analysis of the metallicity of the Magallanic RR Lyrae in the OGLE data). We, therefore, conclude that the two distributions are in agreement with each other, albeit for a few pixels in the OGLE map at low $Y_{\rm MB}$ with depleted star counts, which are likely due to the effects of the survey's footprint.

5.5 Density of the Milky Way's hot corona

Above, we have shown that there are two bridges between the SMC and LMC: a gaseous bridge which contains YMS stars and a bridge containing old stars (e.g. Fig 15). The gaseous bridge trails the old stellar bridge relative to the direction in which the LMC/SMC is moving by ∼5 kpc. Since both bridges connect to the SMC at the same location, it is likely that both bridges come from material stripped from the SMC during the same previous pericentre about the LMC. Interestingly, the relative proper motion of the SMC with respect to the LMC is aligned with the stellar bridge suggesting the bridge is the trailing arm (e.g. Fig 14). In Section 4.1, we hypothesized that the offset between the bridges is likely caused by the additional ram pressure which is being exerted on the gaseous bridge by hot gas in the Milky Way halo (corona). Equipped with the offset in the bridges, Δx, the time since material was stripped, Δt, the relative velocity of the LMC and the MW, $v_{\rm rel}$, and the column density of neutral gas in the bridge, $N_{\rm MB}$, it is possible to roughly estimate the gas density of the hot corona of the Milky Way, $\rho_{\rm cor}$.

The ram pressure on the gaseous bridge is given by $\rho_{\rm cor} v_{\rm rel}^2$. If we consider a block of the gaseous bridge with area dA facing the oncoming gas and length dl, the force on this block from ram pressure is $\rho_{\rm cor} v_{\rm rel}^2 dA$ and the mass of the block is $dM = \rho_{\rm MB} dA dl$. If we further assume that the extent of the gaseous stream perpendicular to its track is roughly similar in both directions, which is justified if it is a stream, then the column density and density of the bridge are related by $N_{\rm MB} \sim n_{\rm MB} dl$, where $n_{\rm MB}$ is the average number density of hydrogen atoms in the bridge. As a consequence, the mass of the gas block is $N_{\rm MB} \mu_{\rm MB} m_{\rm p} dA$, where $\mu_{\rm MB} = 1.33$ is the atomic weight assuming that the gas in the bridge is neutral and that the gas is made up of the universal fractions of hydrogen and helium, and $m_{\rm p}$ is the proton mass. This gives an acceleration of

$$a \sim \frac{n_{\rm cor} \mu_{\rm cor} v_{\rm rel}^2}{N_{\rm MB} \mu_{\rm MB}} \tag{4}$$

where we have written the coronal density in terms of the number density as $\rho_{\rm cor} = n_{\rm cor} \mu_{\rm cor} m_{\rm p}$ with an atomic weight $\mu_{\rm cor} \simeq 0.6$ since this medium is hot and largely ionized (Miller & Bregman 2015). Assuming that the gaseous and old stellar bridge have been exposed to the ram pressure for some time Δt, at the present they will have an offset of

$$\Delta x \sim \frac{n_{\rm cor} \mu_{\rm cor} v_{\rm rel}^2}{2 N_{\rm MB} \mu_{\rm MB}} \Delta t^2. \tag{5}$$

Solving for the coronal number density we find

$$n_{\rm cor} \sim \frac{2 \mu_{\rm MB} N_{\rm MB} \Delta x}{\mu_{\rm cor} v_{\rm rel}^2 \Delta t^2}. \tag{6}$$

Plugging in numbers of $v_{\rm rel} \sim 350$ km s^{-1} (based on the observed proper motion and radial velocity of the LMC), $\Delta x \sim 5$ kpc (from the measured offset), $\Delta t \sim 200$ Myr (from the typical time the simulated LMC/SMC enters the region within 60 kpc of the MW), and $N_{\rm MB} \sim 2 \times 10^{20}$ cm^{-2} from the observed H I column density of the dense part of the bridge as shown in Fig. 15 (see also Putman et al. 2003), we find

$$n_{\rm cor} \sim 3 \times 10^{-4} {\rm cm}^{-3}. \tag{7}$$

This rough estimate is consistent with previous estimates based on ram-pressure effects on Milky Way satellites: $1.3-3.6 \times 10^{-4}$cm^{-3} (Gatto et al. 2013) and $0.1-10 \times 10^{-4}$ cm^{-3} (Grcevich & Putman 2009), as well as estimates based on the distortion of the LMC disc: $0.7-1.5 \times 10^{-4}$ cm^{-3} (Salem et al. 2015). Finally, it satisfies the upper limit for the average electron number density between us and LMC, $\langle n_{\rm e} \rangle \simeq 5 \times 10^{-4}$ cm^{-3}, determined using dispersion measures from pulsars on the LMC (Anderson & Bregman 2010).

Note that this estimate comes with several additional caveats. First, we have assumed that both the old stellar bridge and the gaseous bridge are the trailing tail of the SMC debris while they could, in principle, represent leading and trailing arms of the stream or even different wraps. However, given Fig. 14 which shows that the relative proper motion of the SMC with respect to the LMC is aligned with the old bridge suggesting it is the trailing tail, and the results of Besla et al. (2012) and Diaz & Bekki (2012) which both find that the H I bridge is well modelled by the trailing tail of SMC debris, we think this is a reasonable assumption. Secondly, we have assumed that the H I gas bridge and the old stars are stripped from the SMC with the same velocity. However, the gas in the SMC will feel additional ram pressure from the gas in the LMC so the two bridges may look different even before accounting for ram pressure from the Milky Way gas. Thirdly, we have assumed that the gas in the dense part of the bridge is neutral whereas several authors have found significant fractions (up to 50 per cent) of ionized gas (Lehner et al. 2008; Barger, Haffner & Bland-Hawthorn 2013). However, if we took neutral and ionized gas in equal amounts this would only increase the above estimate by a factor of ∼1.5. Finally, we have assumed that the ram pressure simply displaces the gas relative to the stars. In reality, the high relative velocities will give rise to Kelvin–Helmholtz instabilities and turbulence which will compress and shred the gas, making the gaseous bridge wider and more diffuse. An in-depth understanding of how the H I bridge interacts with the ambient material would require a full hydrodynamical treatment of the system, which is beyond the scope of this paper.

We stress that while this is an extremely simple estimate, it shows that the offset is a powerful probe of the gas density in the Milky Way halo. In the future, realistic hydrodynamic simulations of an LMC/SMC pair accreted on to the Milky Way which address the caveats above should be able to provide much more precise estimates.

5.6 Conclusions

We have used the *Gaia* DR1 photometry catalogue GaiaSource to study the outer environs of the SMC and LMC. As part of our investigation, we demonstrate that genuine variable stars can be detected across the whole sky relying only on the *Gaia*'s mean flux and its associated error. In this work, we concentrate on the sample of candidate Magellanic RR Lyrae identified using GSDR1 data alone. Unsurprisingly, giving the limited information in hand, the sample's completeness and purity are low compared to the data sets where light curve and/or colour information is available. The major stumbling block unearthed as part of our analysis is the spurious variability caused by the (likely) failures of the object cross-match algorithm used for the GDR1 creation. Nevertheless, through a series of tests, we demonstrate that the faint features we discover around the Clouds are bona fide. The results of this work can be summarized as follows.

(i) Even with the GDR1 GaiaSource star counts alone, the outer density contours of the SMC can be shown to twist noticeably, forming a familiar S-shape, symptomatic of tidal stripping. Furthermore, the twist is aligned with the relative proper motion of the SMC with respect to the LMC. Thus, we conjecture that the LMC is the likely cause of the disruption. Using the SMC's proper motion relative to its violent neighbour, we classify the tail pointing towards the Large Cloud as trailing and the one on the opposite side of the Small Cloud as leading.

(ii) The distribution of the RR Lyrae reveals a long and narrow structure connecting the two Clouds. This RR Lyrae 'bridge' joins the SMC exactly where the base of the trailing tail can be seen in the all-star density map described above. To verify the nature of the bridge, we use GaGa, a combination of *Gaia* and *GALEX* photometry. The purity of the GaGa RR Lyrae subset is much higher than that of the original GSDR1 sample thanks to the UV-optical colour cut applied. There are only two prominent structures visible in the GaGa RR Lyrae distribution. The first one is the bridge between the Clouds and the second one is the counterpart of the Northern LMC's extension traced previously by Mackey et al. (2016) and Belokurov & Koposov (2016).

(iii) The GaGa photometry allows for an efficient selection of Young Main Sequence (YMS) stars at the distance of the Clouds. Using the GaGa YMS sample, we build a high-resolution map of a narrow bridge composed of stars recently formed within the neutral hydrogen stripped from the SMC. In agreement with previous studies, e.g. most recently by Skowron et al. (2014), the YMS bridge shows nearly perfect alignment with the H I bridge. However, the RR Lyrae bridge is offset from both the YMS stars and the H I by some $\sim 5^\circ$.

(iv) Assuming a constant absolute magnitude to the GSDR1 RR Lyrae, we study the 3D structure of the bridge. It appears that at many positions along the bridge, two structures at different line-of-sight distances can be discerned, one at the mean distance of the LMC and one with distances evolving smoothly from the SMC to the LMC. Taking into account the evolution of the selection efficiency with magnitude, we estimate that each structure contributes similar number of RR Lyrae around the mid-point of the bridge. Therefore, the RR Lyrae bridge is a composite structure, consisting of two stellar streams, one from the LMC and one from the SMC.

(v) Simulations of the Magellanic in-fall appear to be in a broad agreement with the observations presented here. They also help to clarify some of the uncertainties in the interpretation of the *Gaia* data. At $X_{\rm MB} < -10^\circ$, the RR Lyrae bridge is mostly composed of the SMC stellar debris. This part of the bridge is simply the Cloud's trailing tail, while its leading tail is compressed on the sky and stretched along the line of sight. The simulations confirm that the LMC stars can contribute significantly to the inter-Cloud RR Lyrae density to cause an up-turn of the bridge towards the LMC at $X_{\rm MB} > -10^\circ$. Thus, the above hypothesis that a significant part of the RR Lyrae bridge detected here is an extension of the LMC is reinforced. Curiously, the obvious distance gradient in the LMC leaves the nature of the stellar structure stretching out of the dwarf at constant $G \sim 19$ to $X_{\rm MB} = -15^\circ$ rather enigmatic.

(vi) Our results are consistent with the picture of the Clouds painted with Mira-like stars as presented in Deason et al. (2016). For example, there is strong evidence that, similarly to GSDR1 RR Lyrae, the Mira stars trace the LMC as far as $\sim 20^\circ$ from its centre. Furthermore, an excess of Mira stars is detected in the North, the South and the East of the Large Cloud, thus matching the RR Lyrae sub-structures discussed above. Around the SMC, while no visible bridge connecting the Small Cloud to the Large is discernible, there appear to be groups of Mira accumulating at the ends of the S-shape structure.

(vii) Finally, using the offset between the RR Lyrae and the H I bridges, we provide a back-of-the-envelope estimate of the density of the hot gaseous corona of the Milky Way. Under the assumption that both neutral hydrogen and the stars were stripped from the SMC at the same time, the MW halo ought to have density of the order of $\rho_{\rm MW} \sim 3 \times 10^{-4}\,{\rm cm}^{-3}$ to provide the necessary ram pressure to push the H I gas $\sim 5^\circ$ in the trailing direction. Our calculation is simple, but, importantly, is consistent with previous estimates. We believe, therefore, that if the discovery of the stellar tidal tails of the SMC is confirmed, an improved version of the ram-pressure argument presented here can be used to put tight constraints on the amount of hot gas within the viral volume of the Galaxy.

We envisage that in the nearest future, the true nature of the RR Lyrae bridge uncovered here will be verified with the help of follow-up observations. In fact, this can be done using the data from the *Gaia* satellite itself, i.e. that contained within the Data Release 2, which will provide individual stellar colours as well as robust stellar variability information. Bearing in mind the complex interwoven 3D structure of the debris distribution between the Clouds, it will undoubtedly be beneficial to obtain deep broad-band photometry of the region. This should help to disentangle the individual contributions of the LMC and the SMC. As illustrated above, different numerical simulations of the Clouds' in-fall predict distinct patterns in the line-of-sight velocity space. Therefore, the wide-area spectroscopic survey of the Clouds' periphery will be an important next step in deciphering the history of their interaction. Given the unexpected richness of the GDR1, it is certain that the future *Gaia* releases are bound to be truly revolutionary, not only for the inner Galaxy but also for its outer fringes.

ACKNOWLEDGEMENTS

The authors are indebted to the *Gaia* team in general and in particular to Giorgia Busso, Alcione Mora and Anthony Brown for the swift and expertly support they have been providing. It is a pleasure to thank Gurtina Besla and Justin Read for sharing their wisdom regarding the simulations and observations of the Magellanic H I. We also wish to thank Igor Soszyński for the advice on the OGLE variable star data this study has benefited from.

This project was developed in part at the 2016 NYC *Gaia* Sprint, hosted by the Center for Computational Astrophysics at the

Simons Foundation in New York City and in part at the Dark Matter Distribution in the Era of *Gaia* Workshop, hosted by NORDITA.

This work has made use of data from the European Space Agency (ESA) mission *Gaia* (http://www.cosmos.esa.int/gaia), processed by the *Gaia* Data Processing and Analysis Consortium (DPAC, http://www.cosmos.esa.int/web/gaia/dpac/consortium). Funding for the DPAC has been provided by national institutions, in particular the institutions participating in the *Gaia* Multilateral Agreement.

The authors thank the team of The Parkes Galactic All-Sky Survey for making their data public.

The research leading to these results has received funding from the European Research Council under the European Union's Seventh Framework Programme (FP/2007-2013)/ERC Grant Agreement no. 308024. VB, DE and SK acknowledge financial support from the ERC. SK also acknowledges the support from the STFC (grant ST/N004493/1). AD is supported by a Royal Society University Research Fellowship.

REFERENCES

Anderson M. E., Bregman J. N., 2010, ApJ, 714, 320
Bagheri G., Cioni M.-R. L., Napiwotzki R., 2013, A&A, 551, A78
Balbinot E. et al., 2015, MNRAS, 449, 1129
Barger K. A., Haffner L. M., Bland-Hawthorn J., 2013, ApJ, 771, 132
Battinelli P., Demers S., 1992, AJ, 104, 1458
Belokurov V., Koposov S. E., 2016, MNRAS, 456, 602
Belokurov V. et al., 2014, MNRAS, 437, 116
Besla G., Kallivayalil N., Hernquist L., Robertson B., Cox T. J., van der Marel R. P., Alcock C., 2007, ApJ, 668, 949
Besla G., Kallivayalil N., Hernquist L., van der Marel R. P., Cox T. J., Kereš D., 2010, ApJ, 721, L97
Besla G., Kallivayalil N., Hernquist L., van der Marel R. P., Cox T. J., Kereš D., 2012, MNRAS, 421, 2109
Besla G., Hernquist L., Loeb A., 2013, MNRAS, 428, 2342
Besla G., Martínez-Delgado D., van der Marel R. P., Beletsky Y., Seibert M., Schlafly E. F., Grebel E. K., Neyer F., 2016, ApJ, 825, 20
Bianchi L., Conti A., Shiao B., 2014, Adv. Space Res., 53, 900
Bovy J., 2015, ApJS, 216, 29
Brown A. G. A. et al., 2016, A&A, 595, A2
Busha M. T., Wechsler R. H., Behroozi P. S., Gerke B. F., Klypin A. A., Primack J. R., 2011, ApJ, 743, 117
Carrasco J. M. et al., 2016, A&A, 595, A7
Catelan M., 2009, Ap&SS, 320, 261
Clementini G. et al., 2016, A&A, 595, A133
Deason A. J., Belokurov V., Evans N. W., 2011, MNRAS, 416, 2903
Deason A. J. et al., 2012, MNRAS, 425, 2840
Deason A. J., Belokurov V., Evans N. W., Johnston K. V., 2013, ApJ, 763, 113
Deason A. J., Belokurov V., Koposov S. E., Rockosi C. M., 2014, ApJ, 787, 30
Deason A. J., Belokurov V., Erkal D., Koposov S. E., 2016, MNRAS, in press
Dehnen W., Odenkirchen M., Grebel E. K., Rix H.-W., 2004, AJ, 127, 2753
Demers S., Battinelli P., 1998, AJ, 115, 154
Diaz J. D., Bekki K., 2012, ApJ, 750, 36
D'Onghia E., Fox A. J., 2016, ARA&A, 54, 363
Drake A. J. et al., 2013, ApJ, 763, 32
Fellhauer M., Evans N. W., Belokurov V., Wilkinson M. I., Gilmore G., 2007, MNRAS, 380, 749
Gatto A., Fraternali F., Read J. I., Marinacci F., Lux H., Walch S., 2013, MNRAS, 433, 2749
Gibbons S. L. J., Belokurov V., Evans N. W., 2014, MNRAS, 445, 3788
Graczyk D. et al., 2011, Acta Astron., 61, 103
Graczyk D. et al., 2014, ApJ, 780, 59
Grcevich J., Putman M. E., 2009, ApJ, 696, 385
Hammer F., Yang Y. B., Flores H., Puech M., Fouquet S., 2015, ApJ, 813, 110
Harris J., 2007, ApJ, 658, 345
Harris J., Zaritsky D., 2006, AJ, 131, 2514
Hernitschek N. et al., 2016, ApJ, 817, 73
Hindman J. V., Kerr F. J., McGee R. X., 1963, Aust. J. Phys., 16, 570
Irwin M. J., Kunkel W. E., Demers S., 1985, Nature, 318, 160
Irwin M. J., Demers S., Kunkel W. E., 1990, AJ, 99, 191
Jacyszyn-Dobrzeniecka A. M. et al., 2016, Acta Astron., preprint (arXiv:1611.02709)
Jordi C. et al., 2010, A&A, 523, A48
Kalberla P. M. W., Haud U., 2015, A&A, 578, A78
Kallivayalil N., van der Marel R. P., Besla G., Anderson J., Alcock C., 2013, ApJ, 764, 161
Kunkel W. E., Demers S., Irwin M. J., 2000, AJ, 119, 2789
Lehner N., Howk J. C., Keenan F. P., Smoker J. V., 2008, ApJ, 678, 219
Mackey A. D., Koposov S. E., Erkal D., Belokurov V., Da Costa G. S., Gómez F. A., 2016, MNRAS, 459, 239
Majewski S. R., Nidever D. L., Muñoz R. R., Patterson R. J., Kunkel W. E., Carlin J. L., 2009, The Magellanic System: Stars, Gas, and Galaxies. Vol. 256, Proc. Int. Astron. Union, IAU Symposium, Cambridge Univ. Press, Cambridge, p. 51
Miller M. J., Bregman J. N., 2015, ApJ, 800, 14
Muller E., Bekki K., 2007, MNRAS, 381, L11
Nidever D. L., Majewski S. R., Burton W. B., 2008, ApJ, 679, 432
Nidever D. L., Monachesi A., Bell E. F., Majewski S. R., Muñoz R. R., Beaton R. L., 2013, ApJ, 779, 145
Noël N. E. D., Conn B. C., Read J. I., Carrera R., Dolphin A., Rix H.-W., 2015, MNRAS, 452, 4222
Odenkirchen M. et al., 2001, ApJ, 548, L165
Olsen K. A. G., Zaritsky D., Blum R. D., Boyer M. L., Gordon K. D., 2011, ApJ, 737, 29
Pawlak M. et al., 2013, Acta Astron., 63, 323
Peñarrubia J., Gómez F. A., Besla G., Erkal D., Ma Y.-Z., 2016, MNRAS, 456, L54
Pietrzyński G. et al., 2013, Nature, 495, 76
Putman M. E., Staveley-Smith L., Freeman K. C., Gibson B. K., Barnes D. G., 2003, ApJ, 586, 170
Saha A. et al., 2010, AJ, 140, 1719
Salem M., Besla G., Bryan G., Putman M., van der Marel R. P., Tonnesen S., 2015, ApJ, 815, 77
Schlegel D. J., Finkbeiner D. P., Davis M., 1998, ApJ, 500, 525
Scowcroft V., Freedman W. L., Madore B. F., Monson A., Persson S. E., Rich J., Seibert M., Rigby J. R., 2016, ApJ, 816, 49
Sesar B., Jurić M., Ivezić Ž., 2011, ApJ, 731, 4
Shapley H., 1940, Harvard College Obser. Bull., 914, 8
Skowron D. M. et al., 2014, ApJ, 795, 108
Skowron D. M. et al., 2016, 66, 269
Soszyński I. et al., 2008, Acta Astron., 58, 163
Soszyński I. et al., 2009, Acta Astron., 59, 239
Soszyński I. et al., 2010, Acta Astron., 60, 165
Soszyński I. et al., 2016, Acta Astron., 66, 131
Springel V., 2005, MNRAS, 364, 1105
Tollerud E. J., Boylan-Kolchin M., Barton E. J., Bullock J. S., Trinh C. Q., 2011, ApJ, 738, 102
Torrealba G. et al., 2015, MNRAS, 446, 2251
van der Marel R. P., Kallivayalil N., 2014, ApJ, 781, 121
van der Marel R. P., Alves D. R., Hardy E., Suntzeff N. B., 2002, AJ, 124, 2639
van Leeuwen F., Evans D. W., De Angeli F., Jordi C., Busso G., Cacciari C., 2016, A&A, in press
Véron-Cetty M.-P., Véron P., 2010, A&A, 518, A10
Xue X.-X., Rix H.-W., Ma Z., Morrison H., Bovy J., Sesar B., Janesh W., 2015, ApJ, 809, 144

This paper has been typeset from a TEX/LATEX file prepared by the author.